

# **A review on dissimilar laser welding of steel-copper, steel-aluminum, aluminum-copper, and steel-nickel for electric vehicle battery manufacturing**

**Sadeghian, A. & Iqbal, N.**

Author post-print (accepted) deposited by Coventry University's Repository

**Original citation & hyperlink:**

Sadeghian, A & Iqbal, N 2022, 'A review on dissimilar laser welding of steel-copper, steel-aluminum, aluminum-copper, and steel-nickel for electric vehicle battery manufacturing', *Optics and Laser Technology*, vol. 146, 107595.

<https://dx.doi.org/10.1016/j.optlastec.2021.107595>

DOI 10.1016/j.optlastec.2021.107595

ISSN 0030-3992

Publisher: Elsevier

**NOTICE: this is the author's version of a work that was accepted for publication in *Optics and Laser Technology*. Changes resulting from the publishing process, such as peer review, editing, corrections, structural formatting, and other quality control mechanisms may not be reflected in this document. Changes may have been made to this work since it was submitted for publication. A definitive version was subsequently published in *Optics and Laser Technology*, 146, (2022) DOI: 10.1016/j.optlastec.2021.107595**

© 2021, Elsevier. Licensed under the Creative Commons Attribution-NonCommercial-NoDerivatives 4.0 International

<http://creativecommons.org/licenses/by-nc-nd/4.0/>

Copyright © and Moral Rights are retained by the author(s) and/ or other copyright owners. A copy can be downloaded for personal non-commercial research or study, without prior permission or charge. This item cannot be reproduced or quoted extensively from without first obtaining permission in writing from the copyright holder(s). The content must not be changed in any way or sold commercially in any format or medium without the formal permission of the copyright holders.

This document is the author's post-print version, incorporating any revisions agreed during the peer-review process. Some differences between the published version and this version may remain and you are advised to consult the published version if you wish to cite from it.

## **Highlights**

- Review of the main challenges and scientific contributions
- The relationship between the process parameters and joint properties are explored
- The effect of intermetallic compounds on joint properties is assessed
- The applicability of interlayers and coatings are discussed
- Opportunities for further research in this field are highlighted

**A review on dissimilar laser welding of steel-copper, steel-aluminum, aluminum-copper, and steel-nickel for electric vehicle battery manufacturing**

Amirhossein Sadeghian<sup>\*</sup>, and Naveed Iqbal

*Institute for Advanced Manufacturing and Engineering, Coventry University, CV6 5LZ, UK*

\*Corresponding author. E-mail address: sadeghiana@uni.coventry.ac.uk

# **A review on dissimilar laser welding of steel-copper, steel-aluminum, aluminum-copper, and steel-nickel for electric vehicle battery manufacturing**

## **Abstract**

The electric vehicle (EV) battery systems are complex assemblies of dissimilar materials in which battery cells are connected using several thousand interconnect joints. Every single joint influences the functionality and efficiency of the whole battery system, making the joining process crucial. Laser welding is considered a desirable choice for EV battery manufacturing due to its non-contact nature, high energy density, precise control over the heat input, and ease of automation. However, incompatible thermophysical properties of dissimilar materials used in battery tabs and interconnectors pose a significant challenge for achieving complete metallurgical bonds. Furthermore, the formation of undesirable weld microstructures such as hard and brittle intermetallic compounds (IMCs) substantially undermines the structural, electrical, and thermal characteristics of joints. This paper reviews the fundamental difficulties and latest developments in dissimilar laser welding of steel-copper, steel-aluminum, aluminum-copper, and steel-nickel alloys, the potential joint combinations in EV battery pack manufacturing. The microstructure and common metallurgical defects, as well as mechanical and electrical properties of joints are discussed. In addition, the effects of laser welding process parameters and various interlayers and coatings on the joint properties of EV battery welds are assessed.

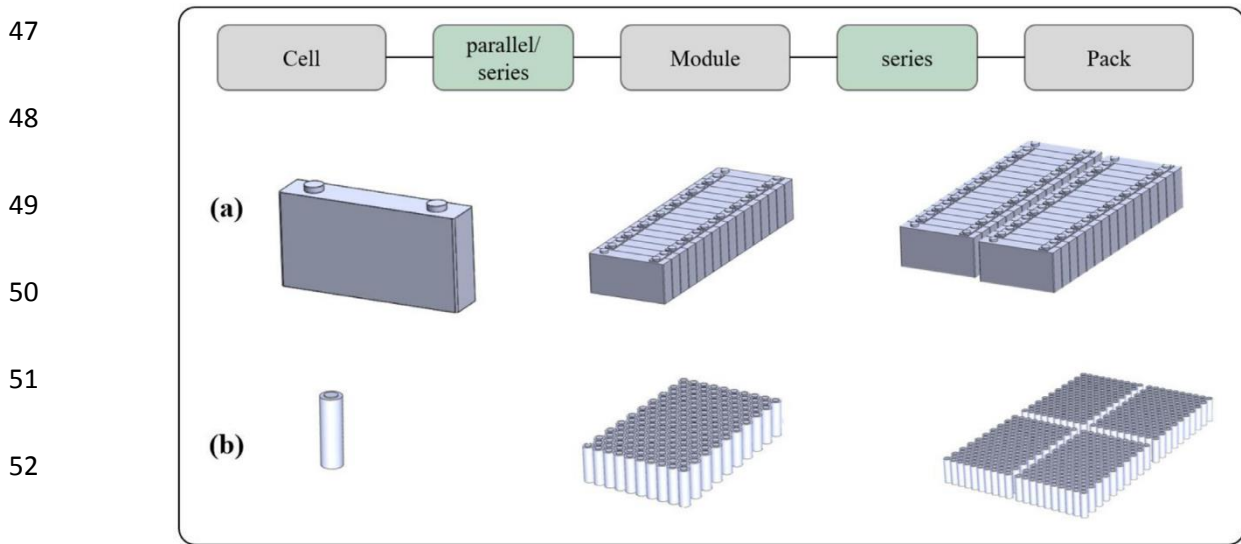
Keywords: Laser welding; Electric vehicle battery; Steel; Copper; Aluminium; Nickel

## **1 Introduction**

The transport sector accounts for 24% of global CO<sub>2</sub> emissions due to the combustion of fossil fuels [1]. It has been reported that internal combustion engine (ICE) vehicles are responsible for almost three-quarters of this amount [2]. Under this threatening situation, carbon emission legislations have been set out across the globe to mitigate the harmful effects of climate change [3,4]. Such policies have prompted nations to modernize the automotive sector and develop electrical vehicles (EVs) to decrease their carbon footprint [5]. The UK, for example, plans to ban the sale of new petrol and diesel cars from 2030 and bring all greenhouse gas emissions to net-zero by 2050 [6]. Similar targets have been set by other major industrialized countries such as China and the EU [7,8].

31 Although EVs offer a promising alternative to conventional vehicles, they only accounted for  
32 2.6% of global car sales and about 1% of the entire global car stock in 2019 [9,10]. The  
33 fundamental barrier to the large-scale adoption of EVs is the limited driving range which combined  
34 with insufficient charging infrastructure can lead to “range anxiety” in EV drivers [11-13]; the fear  
35 of stranding with an empty battery [14]. Currently, most EVs can only go around 100-250 km on  
36 a single charge, much shorter than their ICE counterparts [15]. Using larger batteries is not a  
37 feasible solution owing to limited space in EVs, additional cost, higher weight, and the requirement  
38 of more rare-earth elements [16,17]. Hence, there is a need to enhance the energy density of the  
39 existing battery system as the key component that determines the vehicle’s performance [18,19].

40 Currently, lithium-ion solid-state batteries are the most commonly used source of power for  
41 many low to high-capacity applications, including portable electronics and EVs [20]. While in  
42 mobile devices such as cell phones and laptops only a handful of cells are required, up to several  
43 thousand cells are inter-connected in EV battery systems to deliver the necessary power. Thus, the  
44 cell-to-cell or module level joining is the most critical joining process in battery pack  
45 manufacturing which directly influences the battery capacity [21]. The overview of the EV battery  
46 pack consisting of cell, module, and pack structure is illustrated in Fig. 1.



54 Fig. 1. The EV Battery pack overview with (a) prismatic cells (b) cylindrical cells [21].

55 EV batteries currently use three cell formats: cylindrical, prismatic, and pouch cells (Fig. 2)  
56 [22]. The cell tabs are usually made of aluminum, copper, or nickel and are generally connected  
57 in parallel or series configurations using steel, aluminum, or copper busbars [21]. Weld joints in  
58 EV battery pack involve low-thickness materials (typically 0.3 mm to 1 mm) and the welding  
59 process is normally performed in lap, fillet, or spot configuration [23,24]. A typical joint between  
60 the Al tab and Cu busbar is presented in Fig. 3 [25]. The differences in thermos-physical properties  
61 of dissimilar materials such as melting temperature and thermal conductivity make it difficult to  
62 obtain a complete metallurgical bond without considerable cracks and porosities [26].  
63 Furthermore, the formation of hard and brittle intermetallic compounds (IMCs) at the weld  
64 interface greatly reduces the battery's electrical capacity and structural performance. A weak joint  
65 cannot withstand the harsh driving environments, dynamic loading, vibrations, and possible crash  
66 and might even result in fire due to short-circuiting [27,28]. The presence of IMCs also intensifies  
67 the heat generated during charging and discharging cycles due to their low electrical conductivity  
68 thereby accelerating the degradation process of the battery. The possibility of corrosion due to the  
69 presence of IMCs which deteriorates the joint performance should be considered as well [29].  
70 Atmospheric, localized, crevice, pitting, and galvanic are the most known types of corrosion that  
71 can happen here [30]. Corrosion not only degrades the mechanical performance joints but also  
72 increases the connection's electrical resistance [31]. In summary, a proper joint between cells in  
73 the EV battery system must have the following requirements:

- 74 • Low electrical resistance
- 75 • Good strength
- 76 • High fatigue resistance
- 77 • Low corrosion risk [32,33].

78

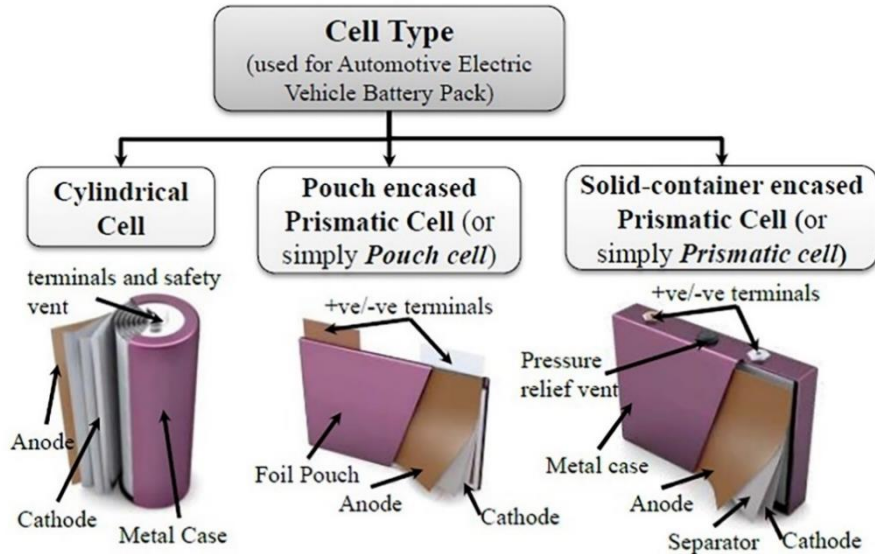
79

80

81

82

83



84

Fig. 2. Cell types used in EV battery pack [20].

85

86

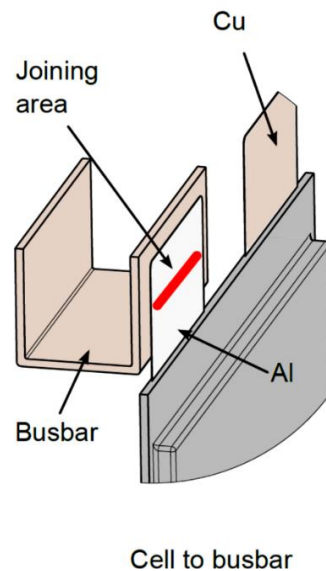
87

88

89

90

91



92

Fig. 3. Joining of Al tab to Cu busbar in pouch cells [25].

93

94

95

96

97

Wire bonding (WB), resistance spot welding (RSW), ultrasonic welding (UW), and laser welding (LW) are the most investigated joining techniques for EV battery manufacturing [21]. Each of these techniques has its advantages and limitations and is used based on cell type, properties, and thickness of the materials involved [20]. Other joining processes such as soldering, friction stir welding, micro-TIG or pulsed arc welding, joining by forming, and adhesive bonding

98 have also been proposed [34-38]. However, due to the lack of information at present, further  
99 research is needed to thoroughly investigate their feasibility [21].

100 In ultrasonic welding, a high-frequency (typically 20 kHz or above) ultrasonic vibration is  
101 applied under pressure to join substrates [20]. Oxides and contamination on the surfaces are  
102 removed during the welding and the result is a metallurgical bond created without melting, based  
103 on diffusion and adhesion of the softened metals [39,40]. UW can produce good welds (without  
104 porosity, hot-cracks, and bulk intermetallics) between highly conductive dissimilar metals, and has  
105 been considered particularly superior for pouch cells. However, it can damage the structural  
106 integrity of cylindrical and prismatic cells due to the high frequency of vibration. It is also  
107 restricted to lap joints [20]. Wire bonding can be defined as single-sided ultrasonic welding of a  
108 small diameter Ag, Cu, or Al wire (typically below 0.5 mm), first to one substrate and then to the  
109 second or more substrates sequentially [22]. It is a technique frequently used in semiconductor  
110 device technology [21], and regardless of no scientific literature on its application in EV battery  
111 manufacturing, wire bonding has been employed in Tesla Model-S to connect battery cells and  
112 busbars [20]. Resistance spot welding is another method that can be used for EV battery welding.  
113 When a high current passes through the interface, it creates localized heating and melting, resulting  
114 in fusion welding of substrates [41]. However, resistance spot welding of highly conductive  
115 materials like aluminum and copper remains challenging and currently, it is only suitable for low-  
116 conductivity materials [20,42]. Laser welding is a highly efficient fusion welding technique with  
117 the advantages of creating a narrow heat-affected zone and a small targeted deformation [43].  
118 Compared to other main welding techniques for EV battery pack manufacturing (i.e., RSW and  
119 UW) the lowest electrical contact resistances and highest joint strengths have been reported with  
120 laser welding [44]. Laser welding has the potential to be used for module-level joining of all three  
121 types of lithium-ion cells [20]. However, A poor metallurgical affinity between dissimilar  
122 materials normally limits the laser welding process and leads to potential defects such as hard and  
123 brittle intermetallic phases and crack sensitivity. Therefore, further investigation is needed in this  
124 area. Studies so far have reported that the joint performance could be improved by optimizing the  
125 welding parameters [45]. Furthermore, the applicability of different interlayers and coatings to  
126 improve joint properties has been the subject of recent investigations [46]. There have also been  
127 recent advances in novel lasers (i.e., blue and green lasers) which allow higher energy absorption  
128 on highly reflective surfaces such as Cu and Al [47,48].



129 This paper presents a comprehensive review on the dissimilar laser welding of the most  
 130 common joint combinations in EV battery system including steel-copper, steel-aluminum,  
 131 aluminum-copper, and steel-nickel. The fundamental metallurgical and structural challenges are  
 132 discussed and the latest developments in process optimization have been highlighted to provide a  
 133 basis for further studies on this topic.

134

## 135 2 Steel-copper

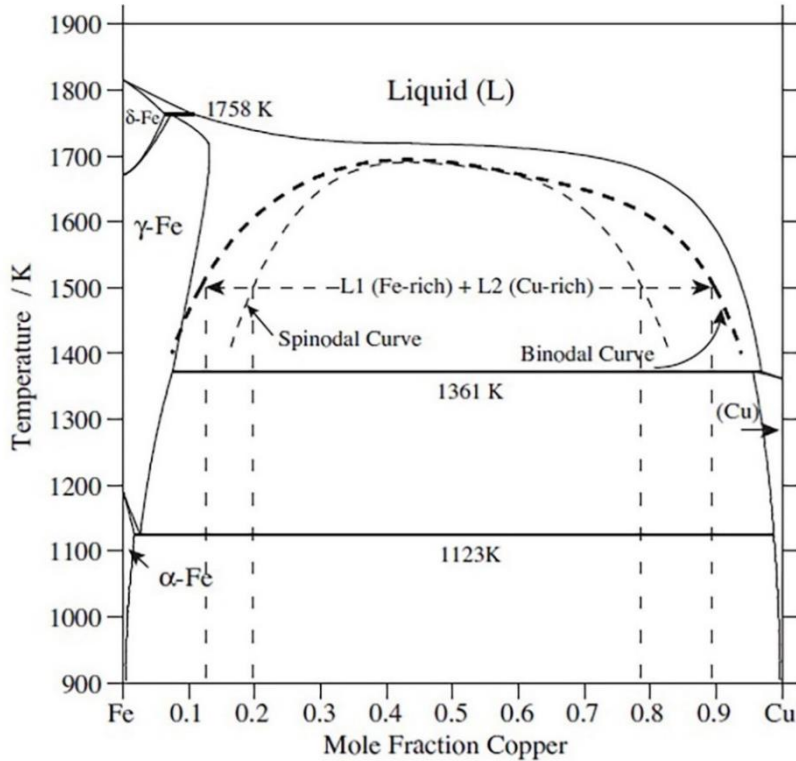
136 The welding of steel to copper is quite common when connecting cells in EV battery systems.  
 137 Table 1 presents the room temperature properties of Al, Cu, Fe, and Ni. While the data is for pure  
 138 metals, they are still useful in understanding the differences in thermos-physical properties of their  
 139 respective alloys. The differences in melting temperatures and thermal conductivities make  
 140 obtaining a complete metallurgical bond very challenging in these systems [49]. In Fe and Cu  
 141 phase diagram, there is a wide metastable miscibility gap at high temperatures (Fig. 4 [50]).  
 142 Separation of the liquid phase is a common feature in laser welding of steel and copper due to  
 143 rapid solidification, as undercooled Fe-Cu liquid separates into droplets of iron and copper [51].  
 144 Another major problem is hot cracking in the weld zone or heat-affected (HAZ) of steel owing to  
 145 Cu penetration into the grain boundaries [52].

146 Table 1

147 Summary of the room temperature properties of Al, Cu, Fe, and Ni [49].

Metal	Melting Temperature (K)	Boiling Temperature (K)	Density (Kg m <sup>-3</sup> )	Thermal Conductivity (W m <sup>-1</sup> K <sup>-1</sup> )	Specific Heat Capacity (J Kg <sup>-1</sup> K <sup>-1</sup> )	Thermal Expansion Coefficient (10 <sup>6</sup> K <sup>-1</sup> )
<b>Fe</b>	1809	3133	7870	78	456	12.1
<b>Al</b>	933	2793	2700	238	917	23.5
<b>Cu</b>	1356	2833	8930	397	386	17
<b>Ni</b>	1728	3188	8900	89	452	13.3

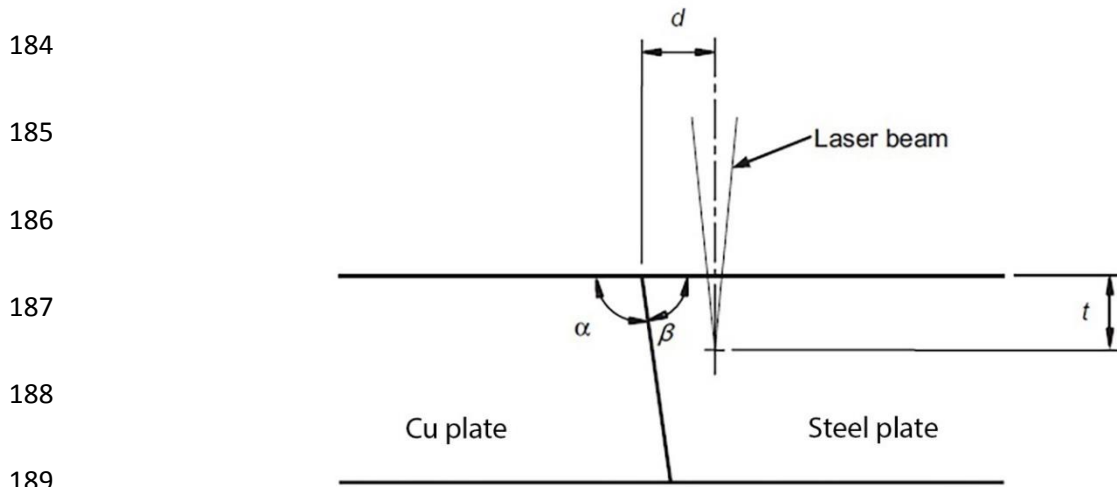
148  
149  
150  
151  
152  
153  
154  
155  
156



157 Fig. 4. The binary Fe-Cu Phase diagram showing the metastable miscibility gap (i.e., binodal  
158 curve) [50].

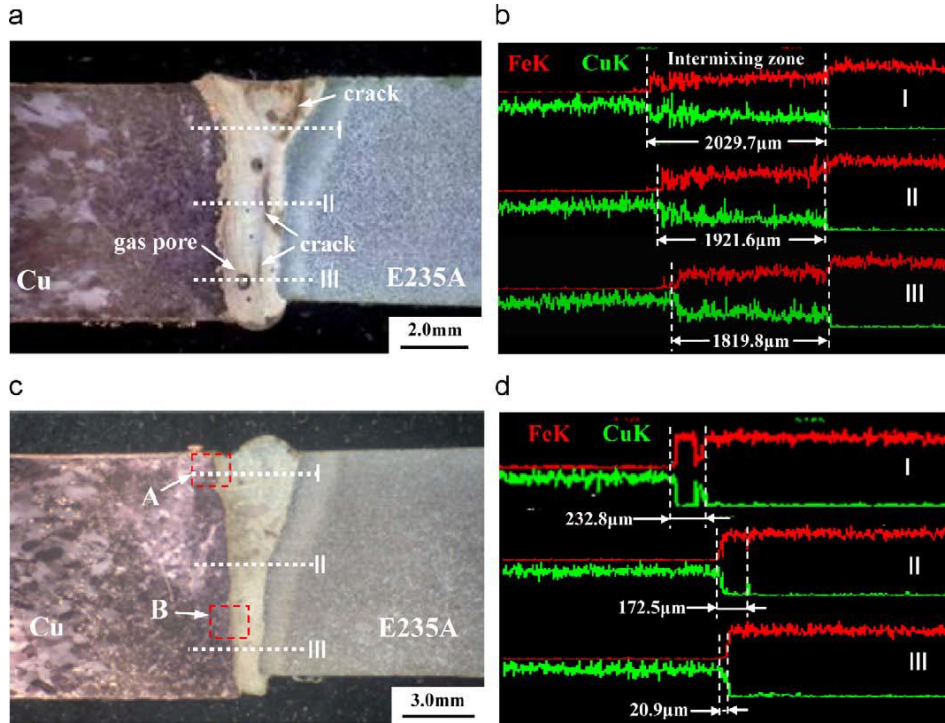
159 Autogenous butt joints between steel and copper have been the subject of several investigations.  
160 Most of these studies focused on laser welding of stainless steel and pure copper. It has been  
161 suggested by some authors that the key to a high-quality joint between copper and steel is reducing  
162 the intermixing of molten steel and copper by keeping the Cu in solid-state mainly by using laser  
163 beam offset or beam deflection towards the steel side. This suppresses the metastable phase  
164 separation during welding, preventing weld cracks and HAZ microfissures [53-55]. Mai and  
165 Spowage [45] produced butt joints between 1 mm medium carbon tool steel and copper by  
166 focusing the beam 0.2 mm towards steel in order to minimize the melting of Cu. While the top of  
167 steel completely melted a lack of fusion was observed between Cu and the weld metal. They  
168 suggested preheating the joint or using a higher power density as possible solutions which can  
169 improve the joint quality. Yao et al. [55] proposed a scarf geometry (i.e., obtuse and acute angles  
170 for copper and steel, respectively) for the butt weld configuration with the laser offset towards  
171 steel. Fig. 5 shows the schematics of this proposed scarf geometry. Plane thickness and laser power  
172 had important effects on the distribution of Cu. Higher thickness (10 mm) and laser power (11KW)

173 reduced the amount of molten copper dissolved in steel compared to the sample with a thickness  
174 of 7 mm and a laser power of 8 KW. Fig. 6a and b illustrate the cross-sectional morphology of  
175 joints with a high dilution ratio of Cu (~36 at%) and the corresponding EDS intensity profiles of  
176 Fe and Cu. The morphology and EDS profiles of the low-dilution (< 1 at%) sample are presented  
177 in Fig. 6c and d, respectively. A complete metallurgical bond without cracks and pores along with  
178 a higher tensile property was achieved for this sample. Cracks and gas pores can be seen in the  
179 high-dilution sample which showed a tensile strength of only 150-200 MPa. An intermixing zone  
180 existed adjacent to the Cu plate in both samples. However, it was narrower in the low-dilution  
181 sample owing to the lower diffusion of Cu. This transition zone consisted of a large number of  
182 granular phases with a composition of Fe-rich bcc solid solution ( $\alpha$ -Fe) and Cu-rich fcc solid  
183 solution (known as the  $\epsilon$  phase) (Fig. 7).



190 Fig. 5. The Scheme of butt configuration with the suggested scarf geometry [55].

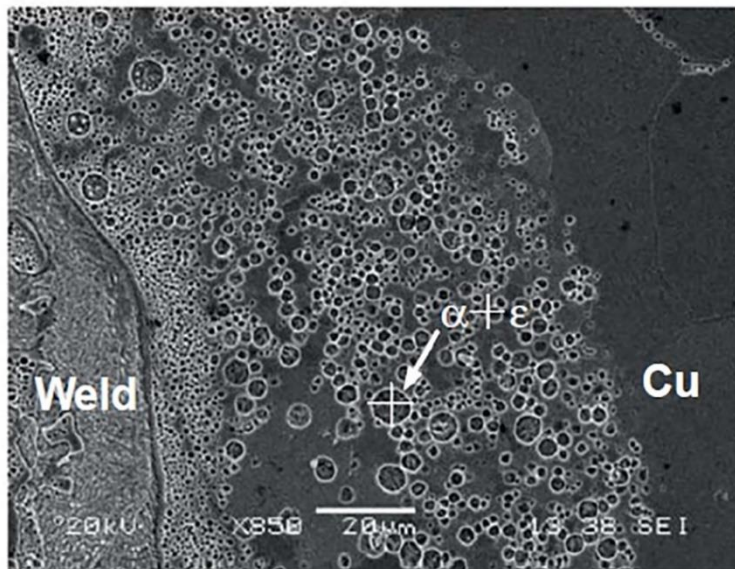
191  
192  
193  
194  
195  
196  
197  
198  
199



200  
201  
202

Fig. 6. a) Microstructure of the joint with a higher Cu dilution (~36 at%), b) EDS line scans of Fe(K) and Cu(K), c) Microstructure of the joint with a lower Cu dilution (< 1 at%), d) EDS line scans of Fe(K) and Cu(K) [55].

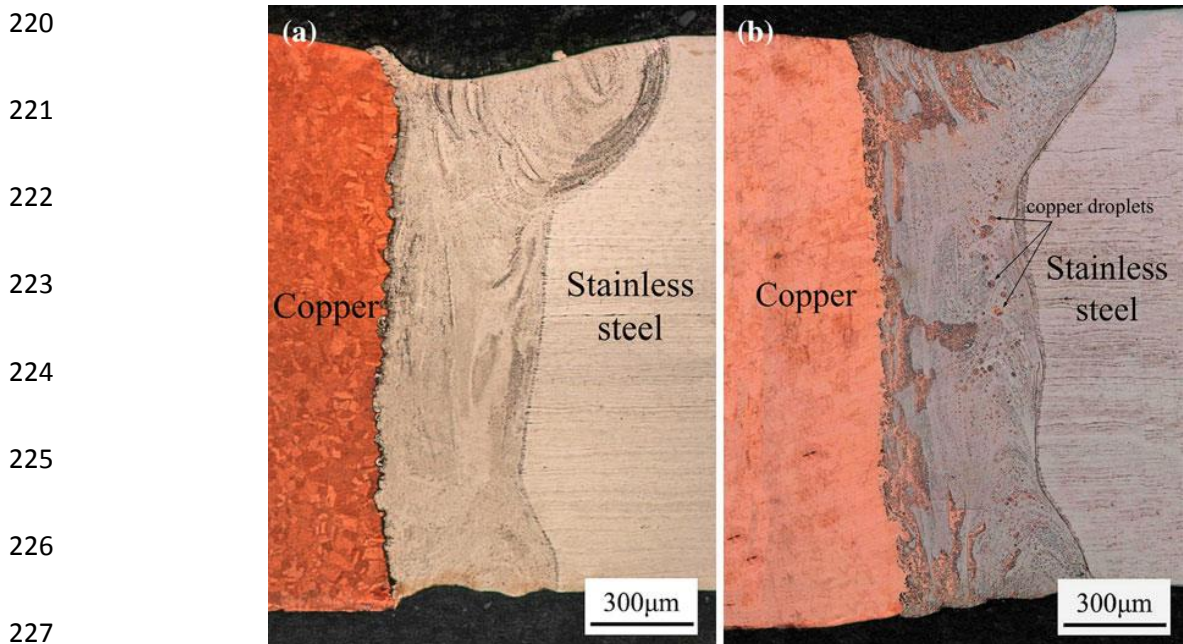
203  
204  
205  
206  
207  
208  
209



210

Fig. 7. Microstructure near the interface between intermixing zone and Cu plate [55].

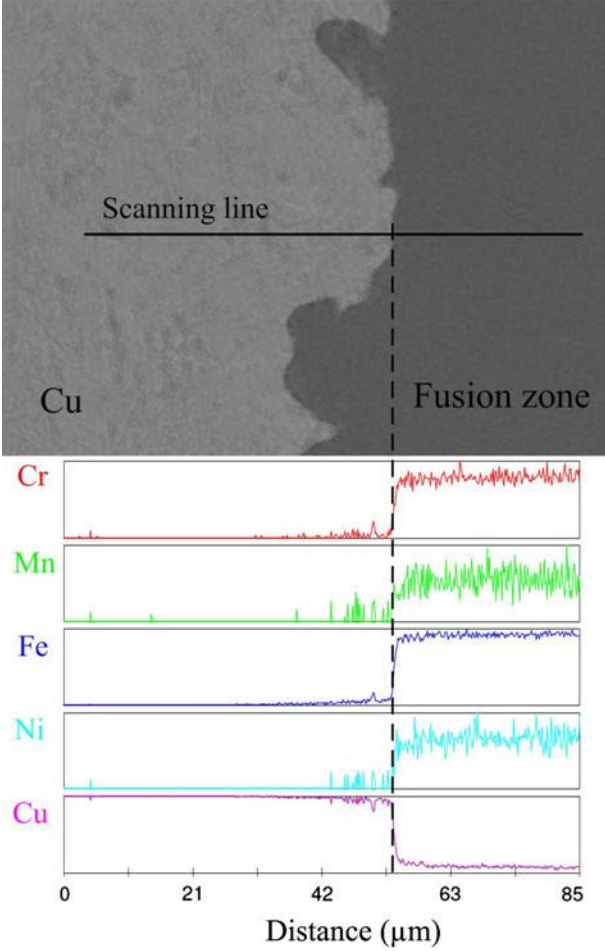
211 Chen et al. [53,56] have reported the microstructural characteristics of laser-welded stainless steel  
212 to copper, using an oblique laser. They stated that laser beam inclination towards stainless steel  
213 could melt stainless steel while keeping the low-melting-point copper in solid-state, resulting in  
214 the “welding-brazing mode”. Owing to the low amount of melted Cu it forms a dilute solution in  
215 the fusion zone. However, excessive beam offset or welding speed should be avoided since can  
216 result in the lack of fusion in the copper and weld zone interface. While in “Welding-brazing  
217 mode”, liquid separation and microcracks in the fusion zone were prevented in “fusion welding  
218 mode” the melt pool entered the metastable miscibility gap and separated into two immiscible  
219 liquids of Cu and stainless steel. These two joining modes are shown in Fig. 8.



228 Fig. 8. (a) welding-brazing mode (beam inclination 0.2 mm towards steel), (b) fusion welding  
229 mode (without beam inclination) [53].

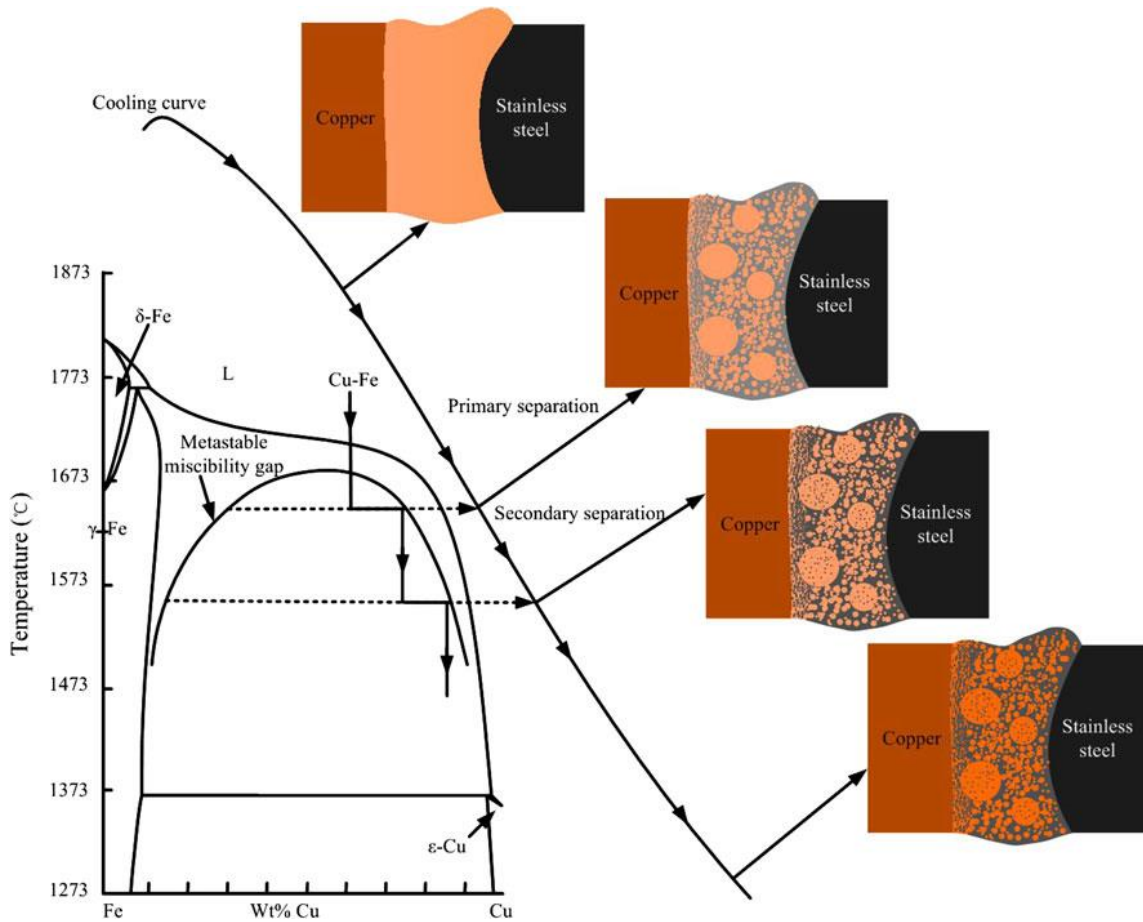
230 A jagged interface was formed between copper and liquid metal owing to the strong fluid flow of  
231 the molten pool during the welding. The composition distribution at the interface during welding-  
232 brazing is presented in Fig. 9. The diffusion of alloying elements of stainless steel (e.g., Fe, Cr,  
233 Mn, and Ni) into copper is an indication of a metallurgical bond between copper and stainless  
234 steel. The combination of scraggly interfacial morphology and metallurgical bonding resulted in  
235 improved mechanical properties in the “welding-brazing” mode.

236  
237  
238  
239  
240  
241  
242  
243  
244  
245  
246



247 Fig. 9. Composition distribution at the interface between copper and stainless steel in “welding-  
248 brazing mode” [53].

249 In “fusion welding mode” when partial melting of copper and mixing with the melt pool occurred,  
250 the liquid underwent primary and secondary separation owing to the high cooling rate and  
251 supercooling of the laser welding process. Fig. 10 illustrates the mechanism of liquid separation  
252 in “fusion welding mode”. Instantly after entering the miscibility gap the liquid underwent the  
253 primary separation creating Fe and Cu liquids. With the lack of full diffusion, the secondary liquid  
254 phase separation occurred as the liquid cooled in the miscibility gap resulting in the supersaturation  
255 of one or both liquids. The final weld microstructure is an inhomogeneous composite of Cu and  
256 stainless steel.



257 Fig. 10. Schematic of liquid separation and its mechanism for fusion welding [53].

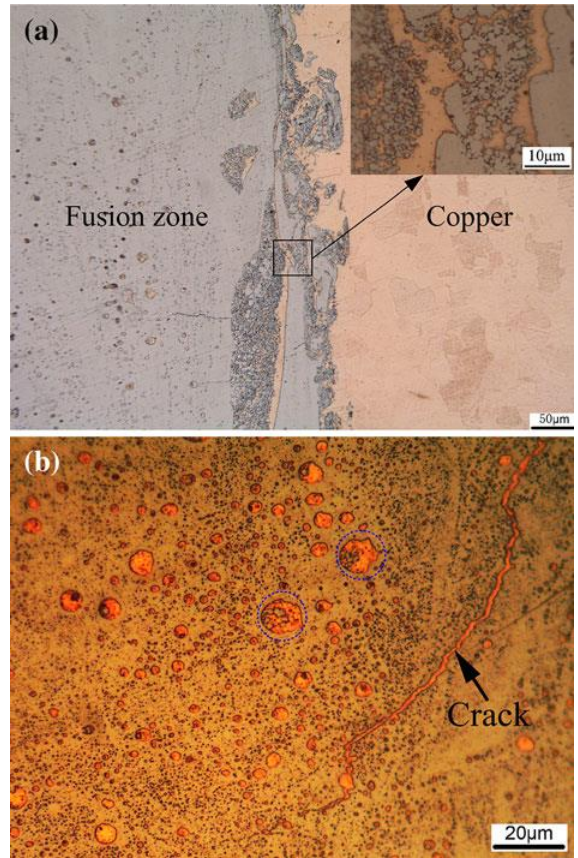
258 Fig. 11 shows the presence of cracks at the weld zone in “fusion welding mode”. These cracks are  
 259 believed to be caused by a thermal stress mismatch between stainless steel and copper. It can be  
 260 seen that copper filled some of these cracks owing to its low melting temperature. A metallurgical  
 261 bond was formed between the crack surfaces and molten copper creating a self-healing property  
 262 thereby reducing the negative effects of cracks. Since some of the cracks were filled with molten  
 263 copper the tensile strength was not influenced because of these cracks. Nevertheless, the toughness  
 264 and fatigue strength decreased with the increase in the amount of molten copper. Thus, they  
 265 maintained that the melting of Cu should be kept at a minimum.

266

267

268

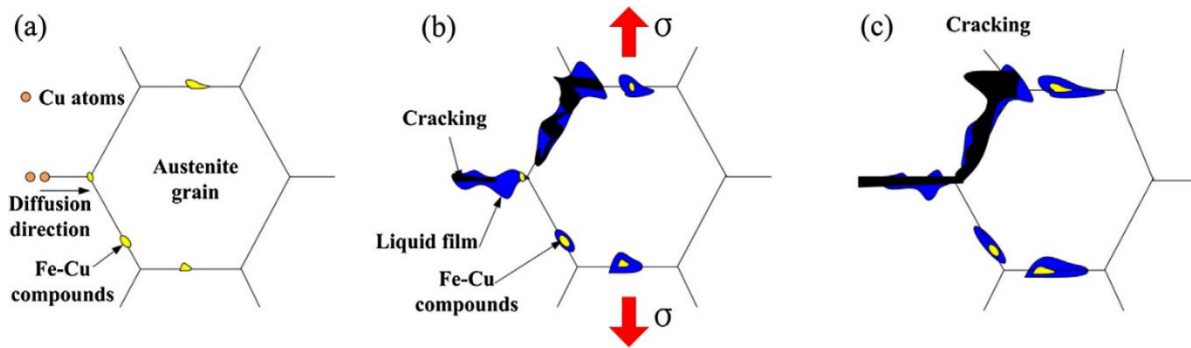
269  
270  
271  
272  
273  
274  
275  
276  
277  
278



279 Fig. 11. Microstructure of the joint in fusion welding mode (a) at the interface, (b) at the fusion  
280 zone [53].

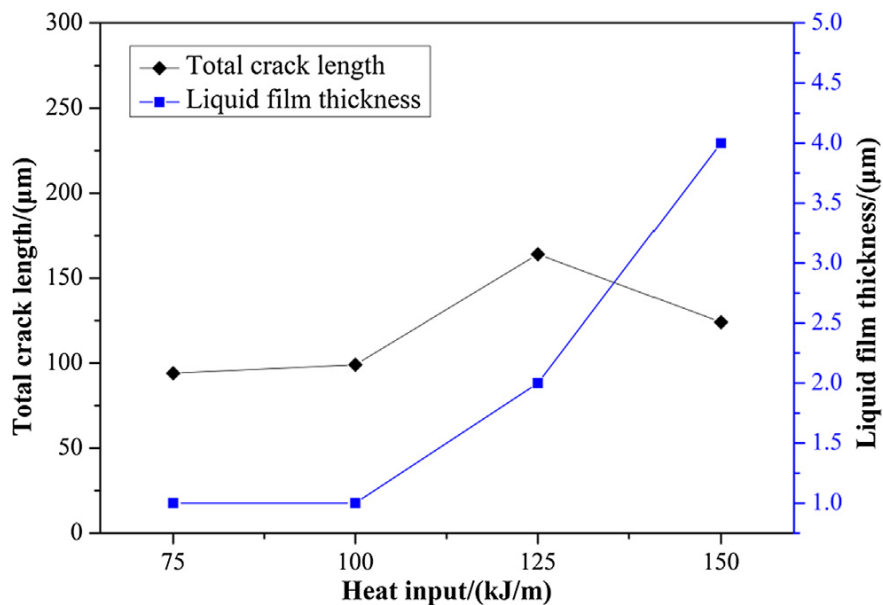
281 Li et al. [57] declared HAZ liquation cracking in the stainless steel and fusion zone porosities as  
282 the two major defects in laser welding of stainless steel and copper. The existence of Fe-Cu  
283 compounds at the HAZ grain boundaries weakened the cohesion between grains and created the  
284 susceptibility to cracks. The three stages of liquation cracking formation are presented in Fig. 12.  
285 The first stage is crack incubation at grain boundaries in which Cu atoms permeated along the  
286 grain boundaries due to a small resistance. In the second stage, crack initiation Fe-Cu compounds  
287 enriched at grain boundaries undermining the cohesion between the grains. Crack growth is the  
288 third and final stage. The thermal stresses increased massively with the increase in heat input  
289 during the laser welding process, leading to the extension of small cracks into forming big cracks  
290 at grain boundaries.





291 Fig. 12. Liquation cracking model (a) incubation (b) initiation (c) growth [57].

292 Fig. 13 illustrates the relationship between heat input and crack length. The crack length was  
 293 increased with increasing the heat input till 125 KJ/m, after which it began to fall. This was  
 294 attributed to the self-healing property of molten copper which filled the cracks. It was believed  
 295 although crack susceptibility could be lowered with self-healing, to control the weld quality the  
 296 heat input should be reduced by increasing the welding speed or lowering the laser power. The  
 297 other major problem, porosities, occurred independently of HAZ liquation cracking. These  
 298 porosities were the results of keyhole instability correlated with fluid flow. They were successfully  
 299 removed by beam deflection toward stainless steel that altered the flow of liquid metal and  
 300 increased the stirring effect during the welding process [57].



308 Fig. 13. The correlation between the total crack length and heat input [57].

309 Kuryntsev et al. [58] laser welded 321 stainless steel and copper using a stainless steel lead-in plate  
310 keeping the Cu in a solid state. By using this method, no cracks or pores were found in the  
311 weldments. The electrical resistance of the welds was also measured which was more than two  
312 times lower than that of stainless steel, indicating a lack of intermetallics in the weld zone. Other  
313 researchers have also reported obtaining sound welds without defects between steel and copper by  
314 minimizing the melting of copper either using beam offset or inclining the laser beam towards  
315 stainless steel [59-62].

316 However, an alternative approach has been explored by researchers such as Shen and Gupta  
317 [63] by putting laser beam towards Cu in laser welding of 316 stainless steel to oxygen-free copper.  
318 They reported that laser welding with the beam focused on the steel side always led to solidification  
319 cracks in the weld zone no matter the welding parameters. Therefore, a focus of 0.4 mm toward  
320 Cu was used. They reported that when weld metal was enriched with copper (80% of copper in the  
321 weld zone) no solidification cracks were detected. Hot crack clusters were observed along the  
322 austenite grain boundaries in stainless steel HAZ. However, a high tensile strength of 312 MPa  
323 was achieved despite the presence of these cracks. Sahul et al. [64] achieved higher values of  
324 tensile strength up to 261 MPa by offsetting the laser beam towards the copper side due to  
325 intermixing of both metals. The microstructure of the welds between AISI 304 and Cu is presented  
326 in Fig. 14. Fine copper dendrites can be observed at the interface between weld and copper. The  
327 interface was also jagged indicating metallurgical bonding. Grain growth was observed in the HAZ  
328 of copper. Furthermore,  $\delta$  ferrite was detected at the interface of stainless steel and weld metal.  
329 Elemental mapping of Cu, Cr, Fe, and Ni are illustrated in Fig. 15. Visible intermixing of elements  
330 can be seen, dark zones originating from 304 stainless steel and brighter ones from Cu.

331

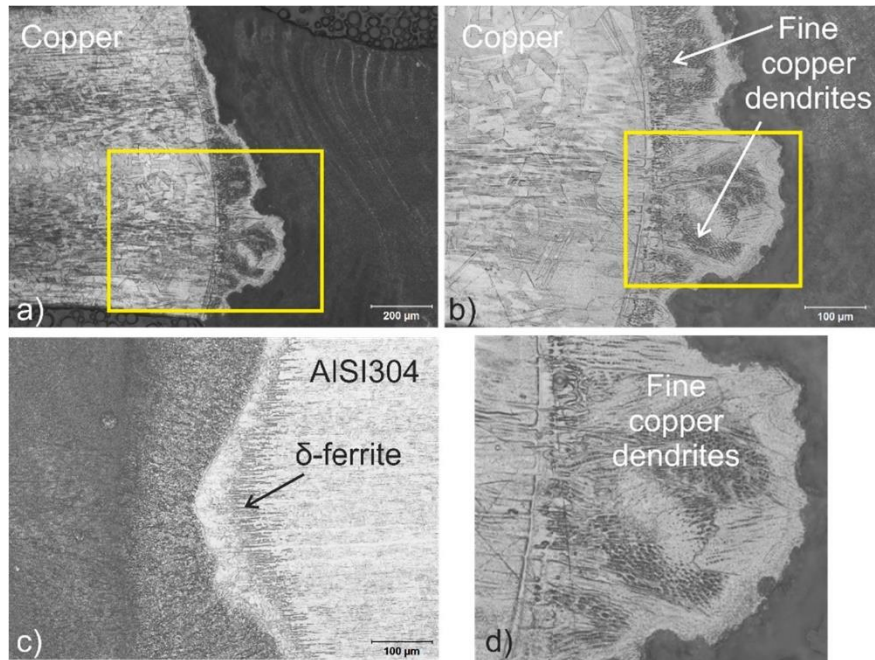
332

333

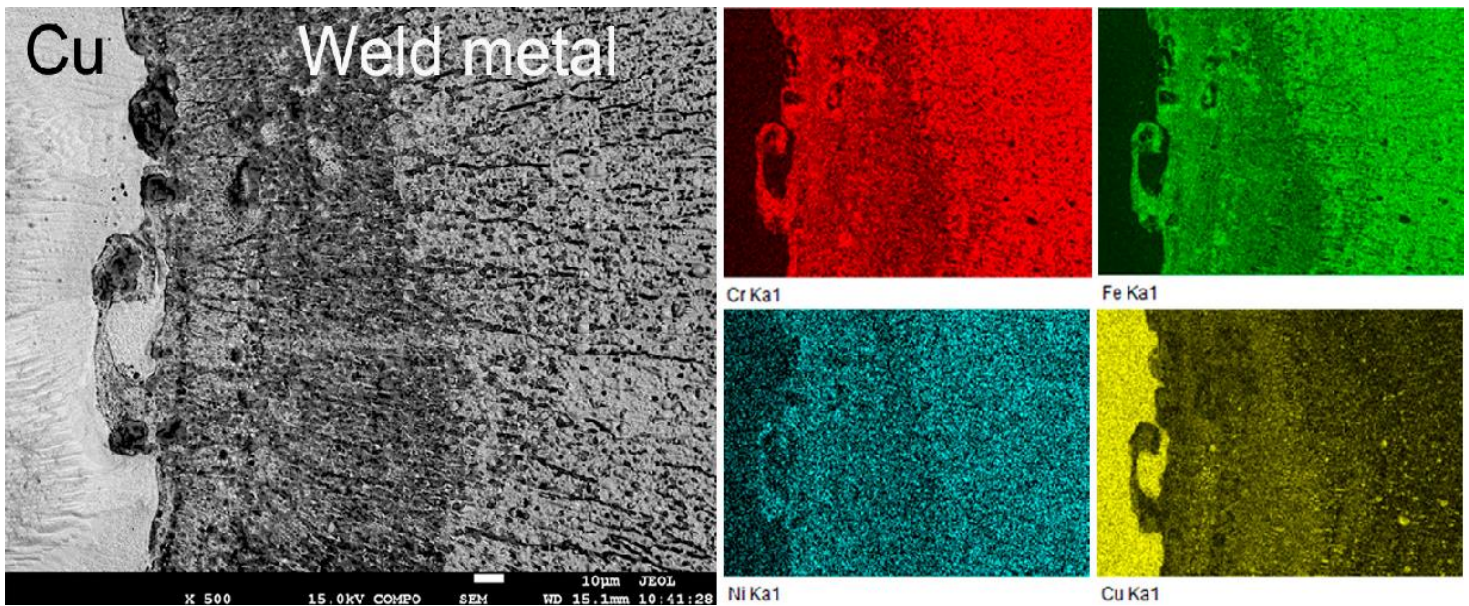
334

335

336  
337  
338  
339  
340  
341  
342  
343



344 Fig. 14. a) Cu-HAZ and weld interface, b) higher magnification of copper-weld metal interface,  
345 c) weld metal-AISI 304 interface, d) fine copper dendrites at higher magnification [64].

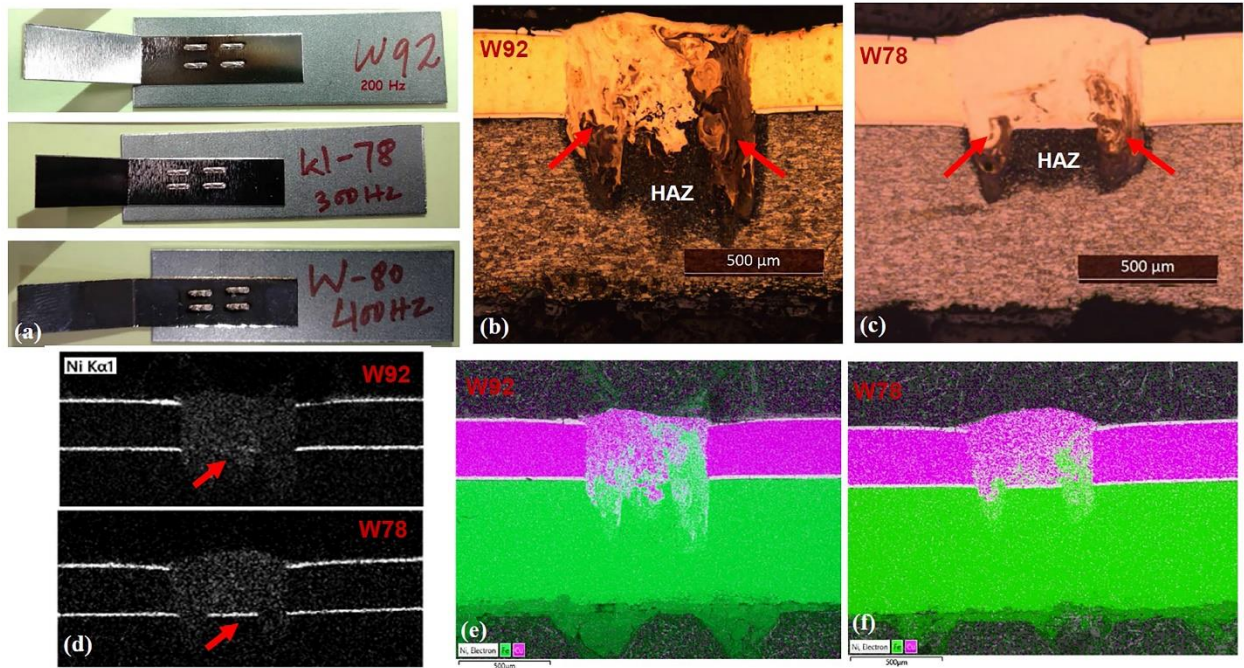


346 Fig. 15. Distribution of elements across the copper-weld metal interface [64].

347 Similarly, Weigl and Schmidt [65] and Joshi and Badheka [66] reported the presence of the  
348 solidification cracks in the “welding-brazing mode”. It was concluded that the presence of Cu  
349 within the weld metal was not responsible for the solidification cracks, and by shifting the beam

350 towards the Cu a higher amount of Cu was melted and participated in the weld resulting in better  
351 static mechanical strength. Joshi and Badheka [66] believed that beam displacement was not the  
352 only way to control solidification cracks. Since compositional gradient within the weld area was  
353 the reason for the cracking, detail works on welding parameters are needed to investigate the  
354 interaction of steel and copper within the weld metal and its effect on solidification cracks.

355 Lap laser welding between steel and Cu has been the subject of a number of studies. Mehlmann  
356 et al. [67] studied the influence of modulation amplitude on laser welding of Ni-plated steel DC04  
357 and bronze CuSn<sub>6</sub>. By using a proper spatial modulation full penetration was achieved thereby  
358 maximizing the strength of the joints. Iqbal et al. [68] compared pulsed arc welding (PAW) and  
359 laser welding for 0.3 mm Ni-coated copper and 0.7 mm mild steel. They used a novel beam  
360 wobbling process to control the weld penetration. Fig. 16 illustrates the effect of laser beam wobble  
361 frequency on the weld microstructure. Higher heat input in the sample with 200 Hz frequency  
362 resulted in complete dissolution of Ni coating while in the sample with 300 Hz frequency the  
363 interface was still visible. By comparing laser welding and PAW, it was observed that laser  
364 welding was able to produce joints with an efficiency of 93% while the weld efficiency for PAW  
365 was limited to 70%. Shaikh et al. [69] investigated laser welding of Ni-coated copper (Cu[Ni]) and  
366 Ni-coated steel (i.e., electrical grade Hilumin) in lap configuration. The effects of laser power,  
367 pulse on time, pulse frequency, and welding speed on the joint properties were studied. Penetration  
368 depth was increased with the increase in laser power. Laser power, pulse on time, and frequency  
369 had a positive correlation with the lap shear strength while speed exhibited a negative correlation.  
370 This was due to the fact that higher power, pulse on time, and frequency resulted in higher  
371 penetration and interface width. The change in electrical resistance and temperature rise was  
372 relatively small in all combinations of process parameter. Electrical resistance and shear strength  
373 followed the same trend. With higher mixing of steel and copper higher strength was achieved  
374 while a slight increase in resistance was also observed (Fig. 17).



375 Fig. 16. (a) Weld samples with different wobble frequencies of 200 Hz, 300 Hz, and 400 Hz (b,c)  
 376 Optical microscopy of 200 Hz and 300 Hz samples (d) EDS image showing Ni coating at the  
 377 weld interface (e,f) elemental distribution in the weld zone [68].

378

379

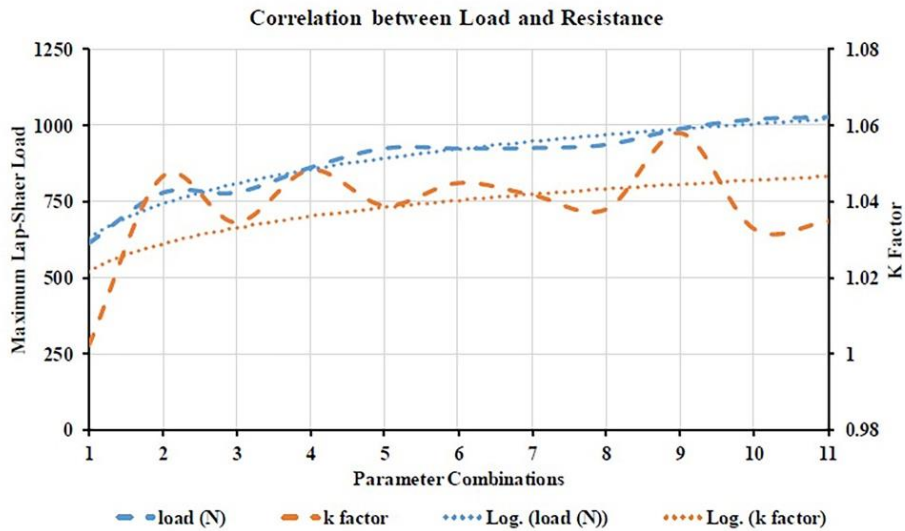
380

381

382

383

384



385

Fig. 17. The correlation between joint resistance and shear strength [69].

386 Table 2 gives a summary of research carried out on dissimilar laser welding of steel and copper.  
 387 Mostly butt joint configuration between stainless steel and copper without interlayers has been  
 388 explored. However, further detailed metallurgical studies are necessary to determine the  
 389 microstructure of the weld zone and the interaction between two materials. Besides, laser welding  
 390 in lap configuration which is widely used in EV battery manufacturing needs more attention. The  
 391 application of potential interlayers or coatings can also be the subject of future investigations.

392

393 Table 2

394 Summary of research conducted on laser beam welding of steel and copper.

Materials	Laser process	Joint type	Optimum laser parameters	Weld characteristics	Max. average tensile strength	Electrical resistance	Ref. (year)
1 mm medium-carbon tool steel/ 1 mm copper	Nd:YAG (Pulse mode)	Butt joint	Beam offset: 0.2 mm towards steel Power: 3.2 KW Speed: 0.2 m/min Pulse frequency: 30 Hz Pulse width: 5 ms	No metallurgical bond between Cu and weld metal - Extensive porosity at the joint interface	Not reported	Not reported	[45] (2004)
4.2 mm 316 stainless steel/4.2 mm copper	Nd:YAG (Pulse mode)	Butt joint	Beam offset: 0.4 mm towards Cu Beam focus: 0.1 mm above the surface Power: 4.8 KW	Hot crack clusters along the austenite grain boundaries in stainless steel HAZ	312 MPa	Not reported	[63] (2004)
10 mm low-carbon Steel (E235A)/10 mm T1 copper	CO <sub>2</sub>	Butt joint	Scarf geometry Bram offset: 1 mm towards steel Power: 11 KW Focus: 4 mm Beam diameter: 0.7 mm	A complete metallurgical bond between steel and Cu - Presence of intermixing zone between Cu and weld metal	233.4 N/mm <sup>2</sup>	Not reported	[55] (2009)

1.2 mm stainless steel/1.2 mm copper	Nd:YAG (Pulse mode)	Butt joint	Power: 3 KW Beam offset: 100 $\mu$ m towards copper	No cracks in the weld area	Not reported	Not reported	[65] (2010)
2 mm 201 stainless steel/2 mm T2 copper	CO <sub>2</sub>	Butt joint	Beam offset: towards Fe Power: 4 KW Beam focus: above the surface	Liquid separation in the weld zone - Rough interfacial morphology between fusion zone and copper - Grain growth in Cu HAZ	Not reported	Not reported	[53] (2013)
0.25 mm Ni-plated DC04 steel/0.2 mm CuSn <sub>6</sub>	Fiber	Lap joint	Power: 170 W Speed: 100 mm/s Amplitude: 0.15 mm	Exceptionally large electrical resistances in the weak welds	~ 500 N	Between 0.3 m $\Omega$ and 0.6 m $\Omega$	[67] (2014)
2 mm 201 stainless steel/2 mm T2 copper	CO <sub>2</sub>	Butt joint	Beam offset: 0.1 mm towards Fe Power: 2 KW Beam focus: above the surface Speed: 1.5 m/min Oblique angle: 2°	Liquid separation in the weld zone - Rough interfacial morphology between fusion zone and copper - Grain growth in Cu HAZ	260 MPa	Not reported	[56] (2015)
3 mm 304 stainless steel/3 mm copper	CO <sub>2</sub>	Butt joint	Beam offset: 50 $\mu$ m towards Fe Power: 3.5 KW Beam focus: at the surface	More curved weld wall on the steel side and straighter (vertical) on the copper side - Narrower HAZ in stainless steel side	201 MPa	Not reported	[60] (2016)
3 mm 321 stainless	Fiber	Butt joint	No beam offset stainless steel lead-in plate	No defects such as pores and cracks - Grain growth in Cu	270 MPa	0.01 $\Omega$	[58] (2017)

steel/3 mm copper			Power: 2.5 KW Speed: 0.6 m/min Beam focus: 12 mm above the surface	HAZ - Intermediate layer between copper and steel			
0.3 mm Ni- plated steel/Ni-plated Copper	Infrared	Lap joint (Cu on top)	Power: 60 W Frequency: 50 Hz Wobble amplitude: 0.4 mm Wobble frequency: 400 Hz Beam focus: above the surface Speed: 0.5 m/min Pulse on time: 2 ms	Maximum interface width of 462 $\mu$ m	1.02 KN	Higher electrical resistivity with more mixing of Cu and Fe	[69] (2019)
3 mm 304L stainless steel/3 mm copper	Fiber	Butt joint	No beam offset Power: 1 KW Frequency: 20 Hz Beam diameter: 2.25 mm Speed: 0.3 m/min	A Jagged interface between Cu and weld metal - Primary and secondary liquid separation	224 MPa	Not reported	[66] (2019)
2 mm 304 stainless steel/2 mm copper C21000	CO <sub>2</sub>	Butt joint	Beam offset: 0.2 mm towards steel Power: 4 KW Frequency: 20 Hz Speed: 1.5 m/min	A negligible amount of Cu in the fusion zone	236 Mpa	Not reported	[62] (2020)
2 mm 304 stainless steel/2 mm T2 copper	Fiber	Butt joint	No beam offset Power: 3 KW Oblique angle: 10° to the side of stainless steel	Polygonal porosity in the wed zone and liquation cracking in stainless steel HAZ	278 MPa	Not reported	[57] (2020)



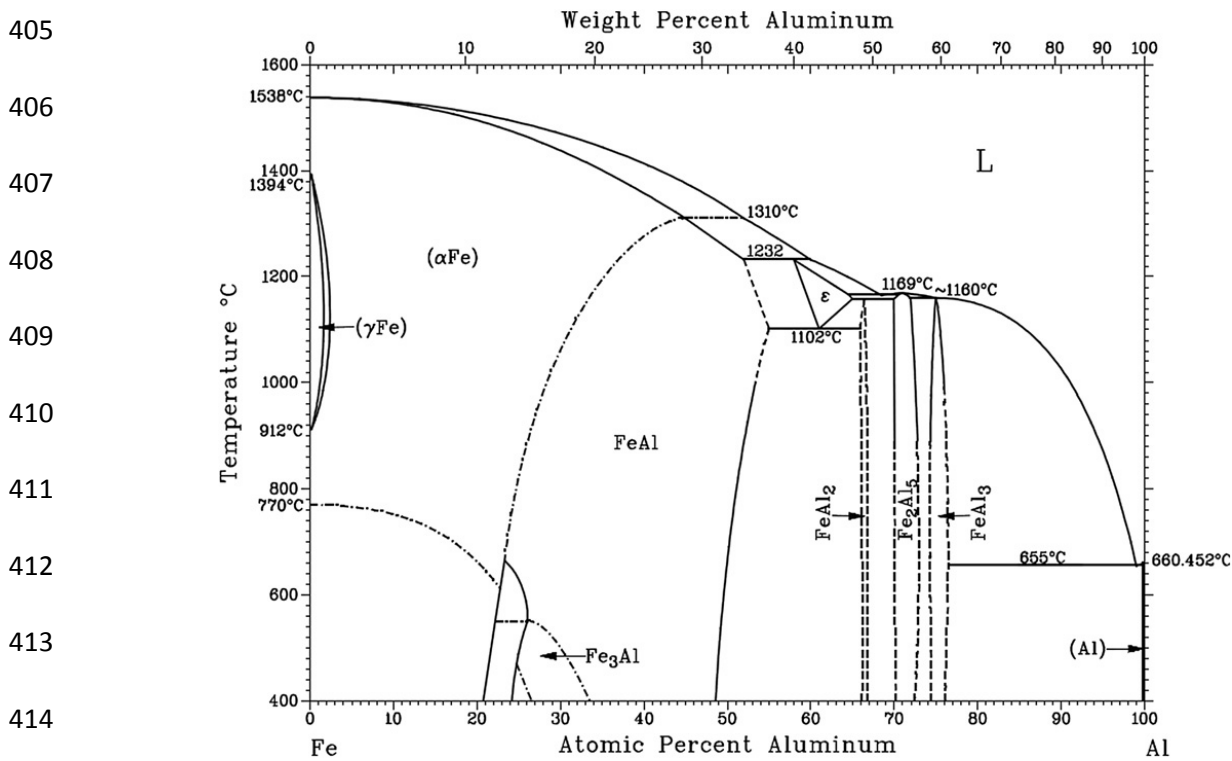
1 mm 304 stainless steel/1 mm copper	Nd:YAG (Pulse mode)	Butt joint	Power: 3.5 KW Beam offset: 50 $\mu$ m towards stainless steel Beam focus: at the surface Pulse duration: 6 ms Pulse energy: 21 J Beam diameter: 0.2 mm Frequency: 10 Hz	Full penetration - the presence of centerline crack - Spatters on the top surface of the weld at the Cu side	146 Mpa	Not reported	[59] (2020)
1 mm 304 stainless steel/1 mm C12200 copper	Disk	Butt joint	Beam offset: 100 $\mu$ m towards Cu Power: 1.3 KW Speed: 1.8 m/min	Elemental intermixing and metallurgical bond	278 MPa	Not reported	[64] (2020)
1.5 mm 304 stainless steel/1.5 mm copper	Nd:YAG (Pulse mode)	Butt joint	No beam offset Power: 2.5 KW Speed: 0.36 m/min Pulse frequency: 20 Hz	Vermicular dendrite and dendrite layer of austenite in the fusion zone	Not reported	Not reported	[61] (2020)
0.7 mm mild steel DC01/0.3 mm Ni-coated copper C110	Fiber	Lap joint (Cu on top)	Pulse frequency: 10 Hz Beam focus: 3 mm above the surface Speed: 100 mm/s Wobble amplitude: 0.6 mm	Cu-Fe composite structure in the weld nugget	660 N	Not reported	[68] (2021)

395

### 396 3 Steel-aluminum

397 The fundamental challenge during laser welding of Al and steel is the formation of brittle  
398 intermetallics that usually include FeAl<sub>2</sub>, Fe<sub>2</sub>Al<sub>5</sub>, and FeAl<sub>3</sub> [70]. Fig. 18 illustrates the equilibrium  
399 phase diagram of Fe-Al. The presence of these intermetallics reduces ductility and affects fatigue  
400 properties. Table 3 presents the hardness of intermetallic components of the Fe-Al system. It can  
401 be seen that Fe-rich intermetallics have much lower hardness compared to Al-rich intermetallics.

402 The optimized heat input to control the melt pool geometry, cooling rate, and solidification  
 403 parameters can potentially help to avoid the formation of the most detrimental intermetallic phases  
 404 and improve the weld strength [71].

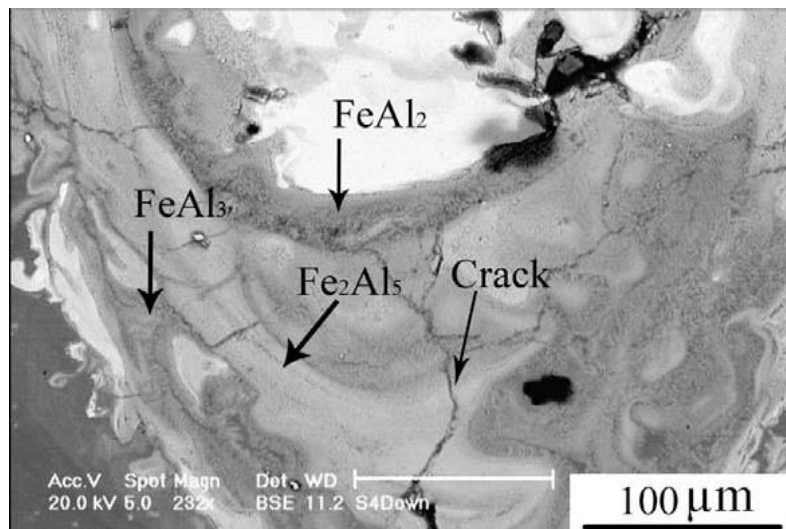


415 Fig. 18. Equilibrium phase diagram of Fe-Al system [72].

416  
 417 Table 3  
 418 Intermetallic compounds in Fe-Al system [73].

Phase	Al content (at.%)	Structure	Microhardness (HV)	Density (g/cm <sup>3</sup> )
Fe <sub>3</sub> Al	25	Ordered BCC	250-350	6.67
FeAl	50	Ordered BCC	400-520	5.37
Fe <sub>2</sub> Al <sub>7</sub>	63	Complex BCC	650-680	NA
FeAl <sub>2</sub>	66-67	Complex rhombohedral	1000-1050	4.36
Fe <sub>2</sub> Al <sub>5</sub>	69.7-73.2	BCC orthorhombic	1000-1100	4.11
FeAl <sub>3</sub>	74-76	Highly complex monoclinic BCC	820-980	3.95

419 The data available in the public domain shows that several attempts have been made to control  
420 intermetallic formation through optimization of process parameters, different heat source modes,  
421 and welding techniques. Torkamany et al. [70] laser welded the 0.8 mm thickness low carbon steel  
422 (ST14) to 2 mm thick aluminum alloy (AA5754), in the overlap configuration. They concluded  
423 that raising the laser power had an adverse effect and created more spatter and intermetallics. The  
424 weld microstructure exhibiting the presence of intermetallics at the bottom of the weld is shown  
425 in Fig. 19. Due to the formation of these intermetallics, crack propagation was observed in the  
426 weld metal and at the weld/Al interface. Increasing the pulse duration also had a similar effect as  
427 higher heat input and resulted in the formation of a large number of intermetallic compounds. On  
428 the other hand, lowering the pulse duration below a critical level resulted in the lack of fusion.  
429 High welding speeds also resulted in incomplete fusion at the interface and reduced joint strength.  
430 They reported optimum values for process parameters that produced high-strength welds as a result  
431 of a low amount of intermetallics, high surface quality, and continuous interface layer without  
432 visible defects. This included a peak power of 1430 W, a pulse duration of 5 ms, and a welding  
433 speed of 4 mm/s.

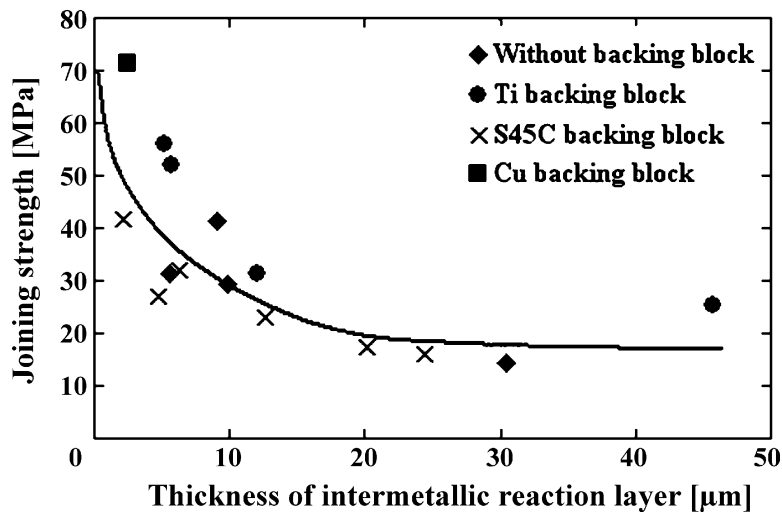


441 Fig. 19. Micrograph of joint microstructure. Intermetallics are seen at the bottom of the weld  
442 near the weld/Al interface [70].

443 Mathieu et al. [74] suggested that the formation of intermetallic phases (e.g., FeAl<sub>3</sub> and Fe<sub>2</sub>Al<sub>5</sub>)  
444 was not the only factor controlling the strength and ductility of the welds especially when their  
445 thickness is below 10 μm. Shrinkage pores and bad cohesion could be detrimental to joint strength.  
446 The global geometry of the welds should be taken into account too. There was a direct relationship

447 between the length of the steel/weld seam and machinal strength. Indhu et al. [75] used a high-  
448 power, pulsed diode laser to join 3 mm thick aluminum alloy AA6061 with 2.5 mm thickness dual-  
449 phase steel DP600. They reported the formation of aluminum-rich intermetallic  $\text{Fe}_2\text{Al}_5$  and  $\text{FeAl}_3$   
450 at the weld zone. A laser power of 4 KW, scanning speed of 5 mm/s, and pulse duration of 10 ms  
451 reduced the thickness of intermetallics. In this case, the maximum intermetallic thickness of  $7\mu\text{m}$   
452 and a minimum thickness of  $1.03\mu\text{m}$  was observed. Jin et al. [76] studied the effect of penetration  
453 depth on the mechanical properties of laser-welded stainless steel SS316L and pure aluminum.  
454 The joint was in lap configuration with steel on top. For the case of higher penetration depth, Al-  
455 rich intermetallics were formed, while for low penetration depth Fe-rich intermetallics were  
456 observed without the presence of any defects thereby enhancing the mechanical properties of the  
457 joints. Pereira et al. [77] investigated the optimal welding parameters based on mechanical and  
458 microstructural investigations. Two sheets of DP1000 steel and aluminum alloy AA1050 of 1mm  
459 thickness were overlap-welded using a pulsed Nd:YAG laser. They reported good quality welds  
460 with tensile strengths close to parent AA1050 when laser power was low enough to prevent full  
461 penetration into Al. Laser welding of low carbon steel DC04 and aluminum alloy AA6016, both  
462 in 1mm thickness, was investigated by Guan et al. [78] using a fiber laser. The focus of their study  
463 was to probe the impact of welding process parameters, on the weld bead geometry and the tensile  
464 strength. They concluded that the welding speed was the main process parameter influencing the  
465 weld properties whereas beam defocus and laser power were secondary factors. Increasing welding  
466 speed reduced the Fe-Al reaction time leading to thinner intermetallics and improved the joint  
467 strength. The optimal laser welding parameter values were reported as laser power of 1400 W,  
468 welding speed 40 mm/s, defocusing 0 mm, and gas flow 35 L/min. A two-pass laser process was  
469 utilized by Ma et al. [79] to produce laser welded joints between 0.75 mm DP590 galvanized steel  
470 and 1 mm 6061 aluminum. The first pass was intended to melt and partially vaporize the zinc  
471 coating whereas the second pass was executed to perform the welding. They declared that laser  
472 power and speed should be adjusted to vaporize the Zn coating but prevent creating extensive  
473 plasma. The best mechanical properties were achieved when the thickness of the Al-rich  
474 intermetallic layer was kept around  $5\mu\text{m}$ . Borrisutthekul et al. [80] investigated the impact of a  
475 backing plate (heat sink) in the suppression of intermetallics formation. Fig. 20 illustrates the  
476 dependence of weld strength on intermetallic thickness. As can be seen, the weld strength increased  
477 with the reduction of intermetallic thickness. They claimed that higher welding speeds and a

478 backing plate with higher conductivity could reduce the thickness of the intermetallic layer leading  
479 to a higher weld strength. They used three different backing blocks; Ti, medium carbon steel  
480 (S45C), and Cu. The best result was achieved with the Cu backing block due to its higher  
481 conductivity which suppressed the generation of intermetallics owing to a higher solidification  
482 rate.



489 Fig. 20. The relationship between intermetallic layer thickness and joining strength [80].

491 Similar results were reported by Pardal et al. [81] for the laser spot welding of steel to aluminum  
492 in the conduction mode. Welds produced with Cu backing plate had a much lower thickness of  
493 intermetallic layer compared to that of Al backing plate, leading to better mechanical properties.  
494 Yan et al. [82] compared a combination of continuous and pulsed dual-beam YAG laser with a  
495 single beam. Continuous-wave heated the materials and created the weld pool while pulse wave  
496 stirred the weld pool. Using this technique, the thickness of the intermetallic layer was reduced  
497 below 10  $\mu\text{m}$ . At the same time, the generation of blowholes or voids was reduced and a deeper  
498 penetration was achieved. Moreover, pulse wave created a root-shaped structure which enhanced  
499 the weld strength (Fig. 21). Shear strength of 128 MPa was achieved for the dual-beam compared  
500 to 71 MPa for single-beam laser-welded samples. Yan et al. [83] tried to improve the  
501 microstructure and performance of steel/aluminum welds by using an external magnetic field. The  
502 XRD results of the phases formed at the weld zone are presented in Fig. 22. It indicates the  
503 presence of Al-rich  $\text{Fe}_2\text{Al}_5$ ,  $\text{FeAl}_3$ ,  $\text{Al}_{192.4}\text{Fe}_{46.22}$ , and a limited amount of Fe-rich  $\text{FeAl}$ , and  $\text{Fe}_3\text{Al}$ .  
504 Adding a magnetic field could alter the content of Fe-rich intermetallics increasing joint strength  
505 and reduce susceptibility to hot cracking.

506  
507  
508  
509  
510  
511  
512  
513

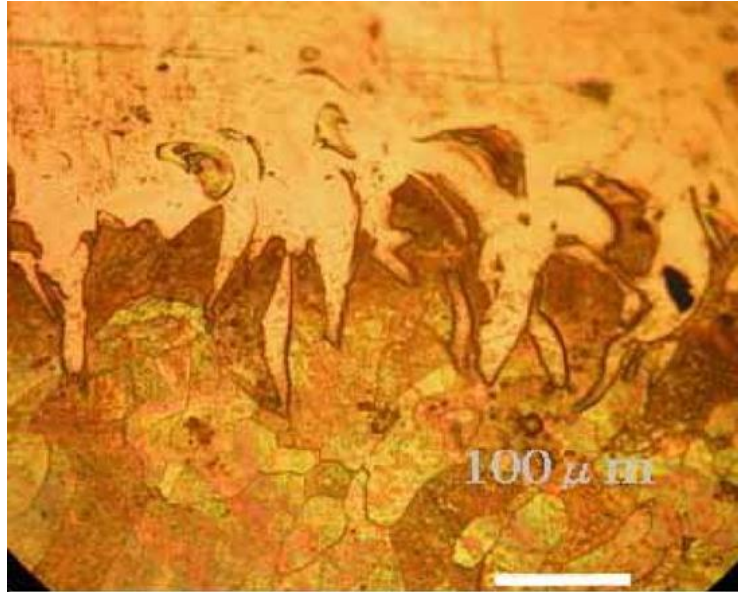


Fig. 21. Root-shape structure at the weld interface [82].

515  
516  
517  
518  
519  
520  
521  
522

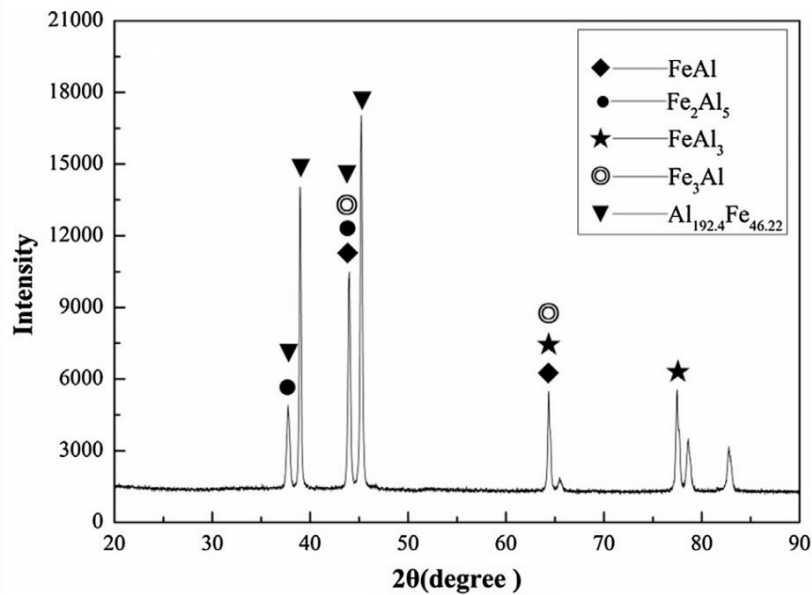


Fig. 22. XRD of laser-welded dual-phase steel and Al 6061 [83].

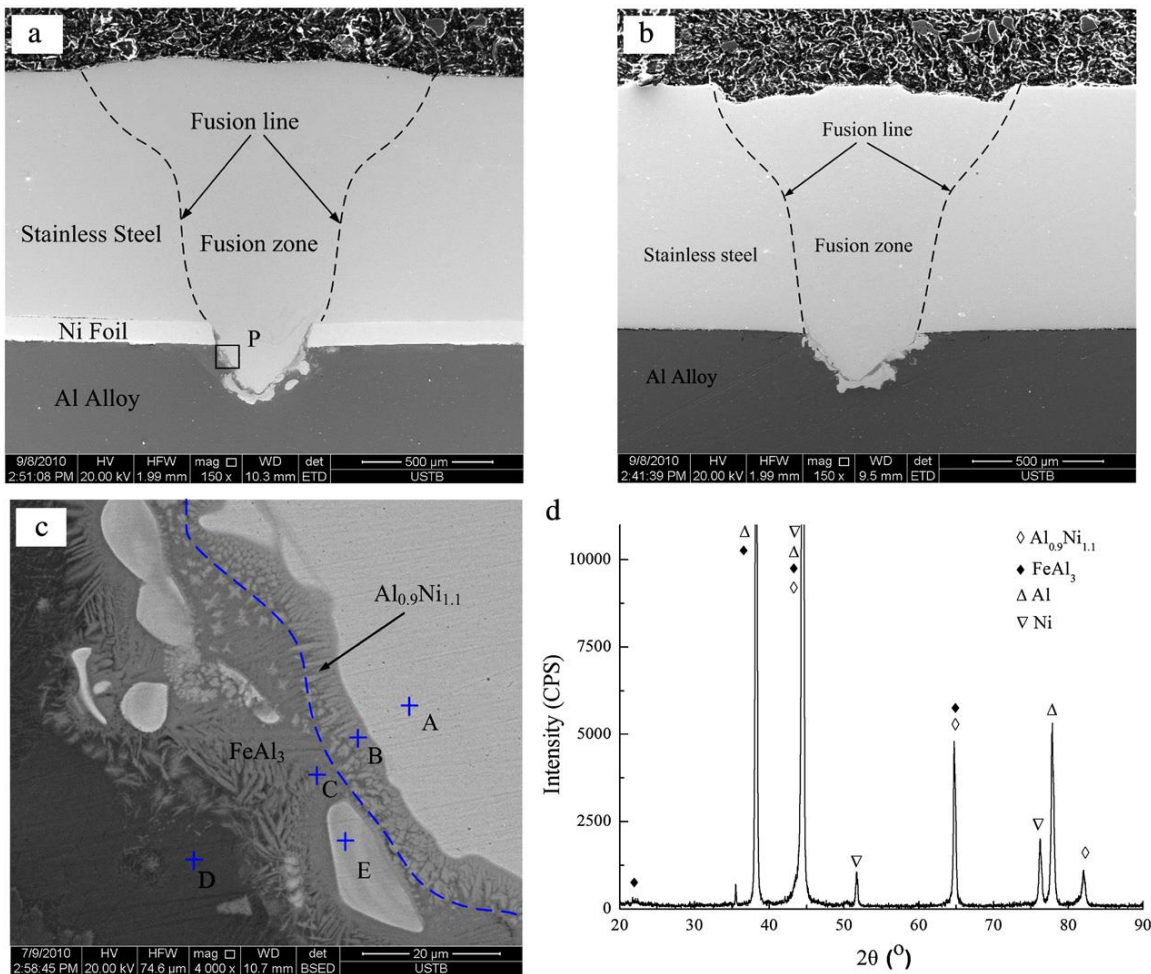
524  
525  
526  
527  
528  
529

Reduction of joint strength due to corrosion is a well-known issue for Al/steel weld couple [84]. Corrosion resistance of AA6016 and hot-dip galvanized steel (DX56D + Z 140 MB) laser joint was studied by Wloka et al. [85]. They used an accelerated corrosion test in a salt spray and microelectrochemical measurements. Both tests showed the joining region as the most susceptible to corrosion. The degree of deterioration depended on the cathodic behavior of adjacent metal. The presence of Fe-containing intermetallics enhanced the corrosion attack due to the strong cathodic

530 behavior. Takehisa et al. [86] investigated the galvanic corrosion of mild steel and AA1100 laser  
531 welded joints by immersion tests in air, distilled water, and salt water. It was revealed that the  
532 effect of galvanic corrosion was stronger in salt water than in distilled water.

533 A relatively novel approach in welding aluminum with steel is using different coatings and  
534 interlayers to tailor the intermetallic formation for improved mechanical properties. It has been  
535 found that transition metal elements like Mn, Zr, Sn, Ni, and Zn have an inhibitory effect on Fe-  
536 Al metallurgical reactions. For example, Jia et al. [87] maintained that the presence of Zinc in  
537 galvanized steel during laser welding/brazing created  $\text{Fe}_2\text{Al}_5\text{Zn}_{0.4}$ , a ductile and tough phase. First,  
538  $\text{Fe}_2\text{Al}_5\text{Zn}_{0.4}$  forms from Al-rich intermetallics  $\text{Fe}_2\text{Al}_5$  and  $\text{FeAl}_3$ , and then zinc atoms diffuse into  
539 Fe-Al phases thereby substituting Fe atoms. Chen et al. [88] studied the effect of a Ni-foil interlayer  
540 during laser welding of A5052 with 201 stainless steel. The weld micrographs, with and without  
541 Ni-foil, are shown in Fig. 23 (a) and (b), respectively. The interfacial microstructure of the sample  
542 with Ni interlayer is shown in Fig. 23 (c), and the corresponding XRD pattern in Fig. 23 (d). The  
543 presence of an intermetallic layer with a thickness of around  $20\mu\text{m}$ , between the fusion zone and  
544 aluminum, is quite visible. This intermetallic layer could be divided into two distinct layers of  
545  $\text{FeAl}_3$  and  $\text{Al}_{0.9}\text{Ni}_{1.1}$  (dotted line in Fig. 23 (c)). This indicated that the Ni-foil altered the  
546 composition of intermetallics. Other elements such as Cr and Mn were present in intermetallics as  
547 solute elements which may generate a positive effect. Some particles of Fe solid solution (zone E)  
548 were detected in the reaction layer but did not change the intermetallics owing to the suppression  
549 of diffusion during the high-speed heating/cooling cycle of laser welding. The authors maintained  
550 that intermetallics were not observed inside the fusion zone as aluminum mixed into molten steel  
551 as a solute element owing to Al having a certain level of solubility in  $\alpha\text{-Fe}$ . The penetration depth  
552 into aluminum had a significant effect on the mechanical properties of the welds. Initially, the  
553 tensile strength increased with the weld penetration up to  $300\mu\text{m}$ , however it then started to  
554 decrease with further increase in penetration depth due to the formation of more brittle  
555 intermetallics with a higher percentage of Al. Furthermore, tensile testing and microhardness  
556 measurements of weld samples revealed that the Ni foil improved the tensile strength while  
557 reducing the microhardness of the intermetallic layer. The tensile strength and microhardness  
558 measurements are shown in Fig. 24 (a) and (b), respectively. In another study, Chen et al. [46]  
559 investigated the effect of Cu interlayer on dissimilar laser welding of Q235 low-carbon steel 5052  
560 Al alloy. The Fe-Al interface mainly consisted of  $\alpha\text{-Al}$  and  $\text{Al}_2\text{Cu}$  eutectic structure,  $\text{FeAl}$ ,  $\text{FeAl}_2$ ,

561 a certain amount of Al-Cu intermetallics,  $\text{Fe}_2\text{Al}_5$ , and  $\text{FeAl}_3$ . The Al-Cu interface mainly consisted  
 562 of the eutectic phase  $\text{Al}_2\text{Cu}$  and the metastable phase of Al-Cu intermetallics. They concluded that  
 563 the addition of Cu interlayer might improve the metallurgical reaction but the  $\text{Al}_2\text{Cu}$  may have a  
 564 detrimental effect on the mechanical property that needs further study. They also compared single  
 565 beam and dual beam lasers. It was observed that with dual-beam laser better process stability and  
 566 greater weld width could be achieved leading to higher tensile strength.



567 Fig. 23. Joint microstructure of stainless steel/aluminum joint a) with Ni interlayer, b) without Ni  
 568 interlayer, c) interfacial microstructure, d) XRD pattern [88].

569 Zhou et al. [89] compared the use of Pb and Cu interlayer in laser welding of DC5D + ZF  
 570 galvanized steel and 6016 Al alloy. Both Cu and Pb interlayer enhanced the tensile strength and  
 571 elongation of joints. However, Pb was better than the Cu joint with a tensile strength of 73.51 MPa  
 572 and elongation of 2.37% compared to 49.44 MPa and 1.3% for Cu. In the case of the Pb interlayer,  
 573  $\text{Mg}_2\text{Pb}$  was formed at the steel/Al interface, and since it was more stable than FeAl the mechanical



574 properties significantly improved. In another study, Zhou et al. [90] compared Mn, Zr, and Sn  
 575 powder. Fig. 25 illustrates the shear strength of joints with and without powder addition. As can  
 576 be seen, the best result belonged to Sn (62.17 MPa) owing to the formation of the FeSn phase  
 577 which similar to  $Mg_2Pb$  was more stable than FeAl. Yang et al. [91] compared pure Al, Al-Si, and  
 578 Zn-Al interlayers. Si was successful in suppressing the growth of the reaction layer. With the  
 579 reduced reaction layer the fracture load improved. While with Zn-Al filler metal the reaction layer  
 580 thickness increased to 38  $\mu m$  the lower microhardness compared to pure Al improved the fracture  
 581 load.

582

583

584

585

586

587

588

589

590

591

592

593

594

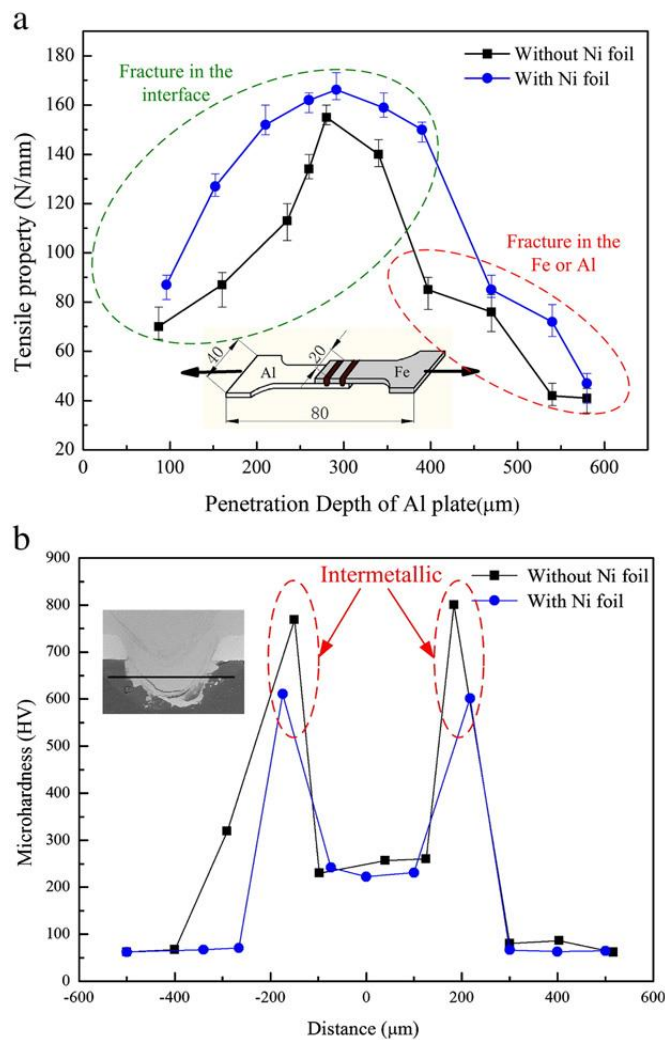


Fig. 24. a) Tensile strength, b) microhardness of the joints [88].

595  
596  
597  
598  
599  
600  
601  
602  
603  
604  
605  
606  
607  
608  
609  
610  
611  
612  
613  
614  
615  
616

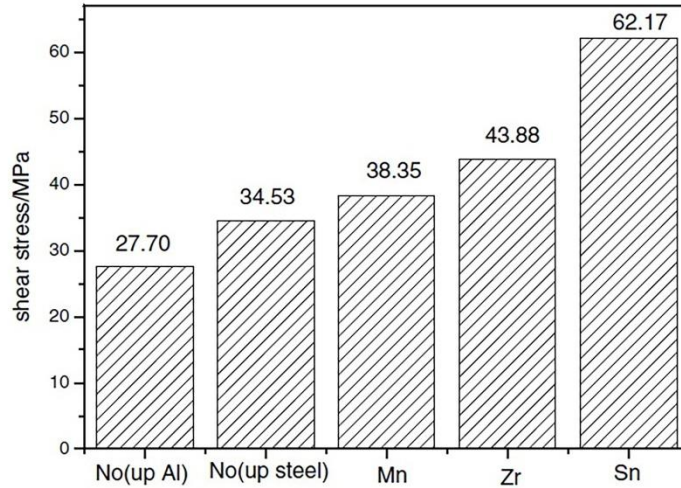
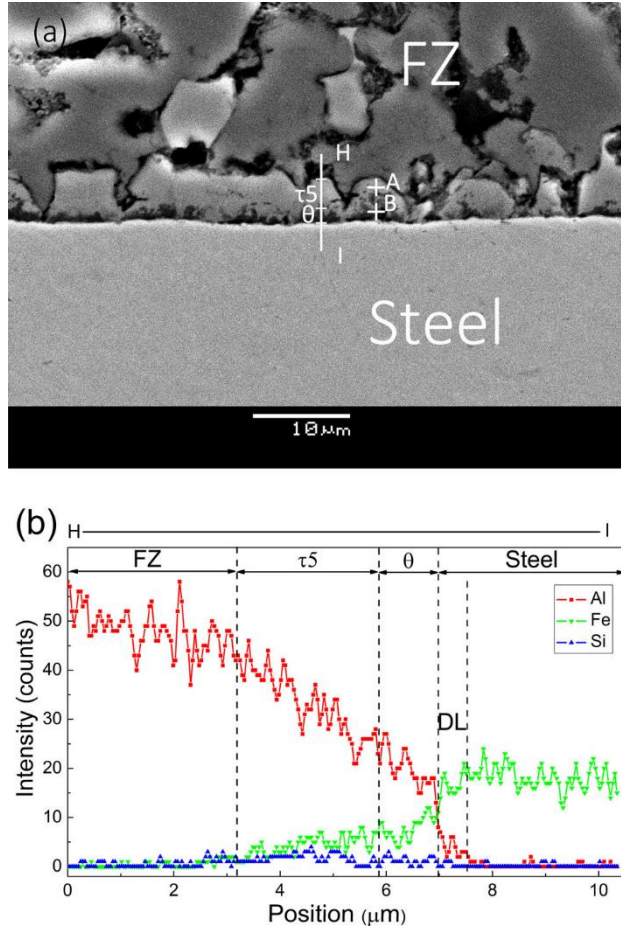


Fig. 25. The average shear strength with and without powder addition [90].

Sun et al. [92] claimed that laser welding/brazing of AA6013 and Q235 low-carbon steel was possible in butt configuration using Al-based ER4043 filler metal. However, due to the formation of brittle Fe<sub>2</sub>Al<sub>5</sub> and FeAl<sub>3</sub> phases, only a joint strength of 120 MPa was achieved. Sierra et al. [93] used the Al-12Si filler wire in laser welding/brazing of AA6016 with low-carbon steel (DC04) to investigate the effect of Si on the growth kinetics of Fe-Al intermetallics. Low-thickness (<2 μm) Fe-Al-Si intermetallics with promising mechanical properties were formed at the weld/steel interface. Yang et al. [94] declared the presence of two distinct intermetallics, τ<sub>5</sub>-Al<sub>7.2</sub>Fe<sub>1.8</sub>Si and θ-Fe(Al,Si)<sub>3</sub> at the weld/steel interface in laser welding/brazing of Zn-coated DP980 steel and AA5754-O with low laser power. The presence of these intermetallics can be seen in Fig. 26. It was observed that due to low heat input the wettability of filler metal was poor. At high laser power, microcracks along with a new planar intermetallic (η-Fe<sub>2</sub>(Al,Si)<sub>5</sub>) were detected owing to a longer time for Fe atoms to diffuse and dissolve. The hard and brittle nature of this intermetallic reduced the joint strength. The best result was achieved at medium laser power in which only θ and τ<sub>5</sub> phases were formed while the wettability was improved resulting in a desirable failure at Al/fusion zone interface.

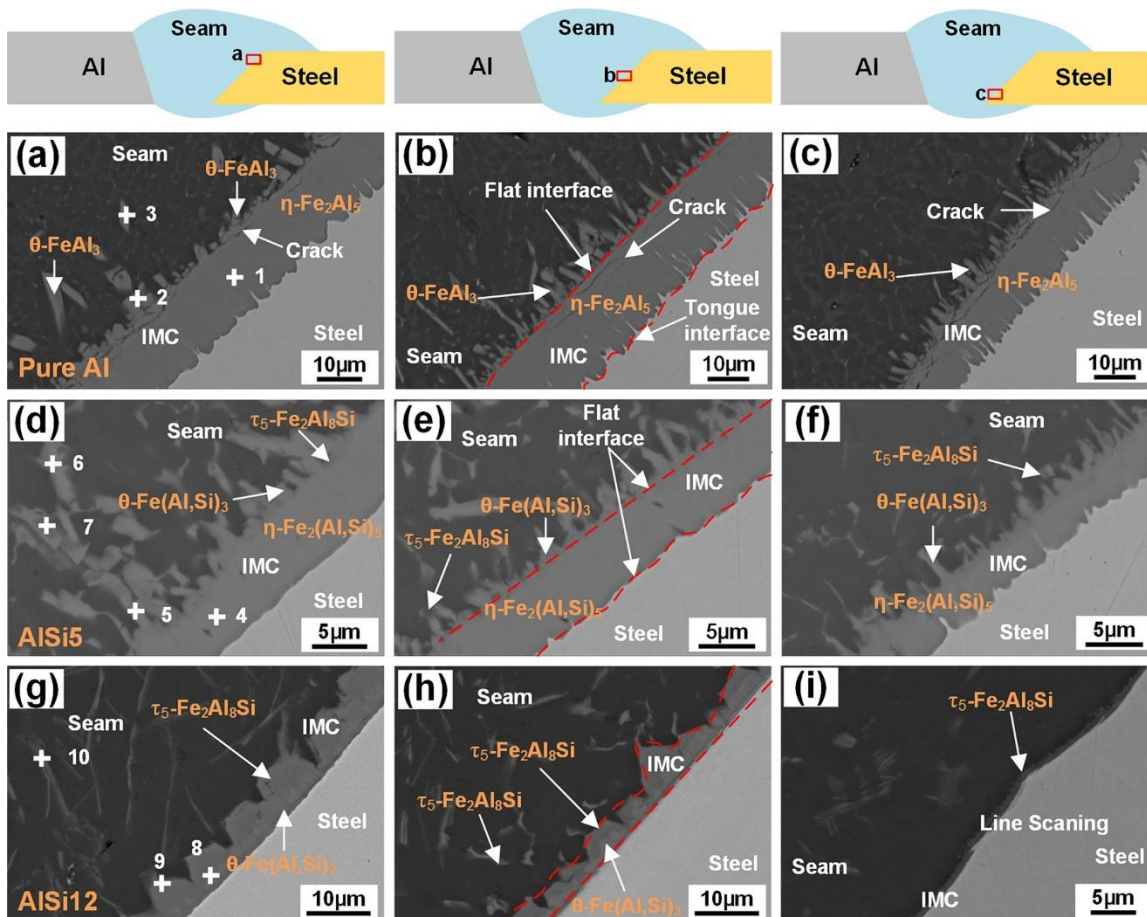
617  
618  
619  
620  
621  
622  
623  
624  
625  
626  
627



628 Fig. 26. (a) The interfacial microstructure of joint at a low laser power (b) EDS line scan [94].

629 Zhang et al. [95] studied the laser welding-brazing of galvanized steel H220YD to aluminum alloy  
630 AA6016 using an Al-5Si interlayer. They reported the thickness of intermetallic ranging from  
631 1.3 μm to 13 μm and composed of  $\alpha(\tau_5)$ -Al<sub>8</sub>Fe<sub>2</sub>Si,  $\theta$ -Al<sub>13</sub>Fe<sub>4</sub>, and  $\zeta$ -Al<sub>2</sub>Fe phases. When the  
632 thickness of  $\theta$ -Al<sub>13</sub>Fe<sub>4</sub> and  $\zeta$ -Al<sub>2</sub>Fe was higher than 10 μm, the joint strength was significantly  
633 reduced. The effect of Si content on the reaction layer was studied by Xia et al. [96] in laser welded-  
634 brazed 6061-T6 Al and DP590 steel using pure Al, Al-5Si, and Al-12Si. The addition of 5 wt.%  
635 Si reduced the thickness of  $\eta$ -Fe<sub>2</sub>(Al,Si)<sub>5</sub> and  $\theta$ -Fe(Al,Si)<sub>3</sub> intermetallic layer owing to the  
636 reduction of elemental diffusion area. 12 wt.% Si altered the intermetallic components to  $\eta$ -Fe<sub>2</sub>Al<sub>5</sub>  
637 and  $\tau_5$ -Al<sub>8</sub>Fe<sub>2</sub>Si and removed  $\eta$ -Fe<sub>2</sub>(Al,Si)<sub>5</sub> (Fig. 27). The strength of joints produced with pure Al  
638 interlayer was lower than of Al-Si filler metal. Moreover, the addition of Si reduced the required  
639 laser power during laser welding/brazing process. The highest tensile strength (208 MPa) and  
640 ductility were attained with Al-5Si due to proper thickness (3.8-7.5 μm), components ( $\eta$ -

641  $\text{Fe}_2(\text{Al,Si})_5 + \theta\text{-Fe}(\text{Al,Si})_3$ ), and the lower hardness of Si in intermetallics. This suggested that  $\eta\text{-Fe}_2(\text{Al,Si})_5$  had higher strength and ductility than  $\theta\text{-Fe}(\text{Al,Si})_3$  phase.



643 Fig. 27. Microstructure obtained with (a-c) pure Al (d-f) Al-5Si (g-i) Al-12Si [96].

644 Despite significant technological advances and extensive research on laser welding of  
 645 aluminum to steel during the past four decades, it is still not widely applied mostly owing to  
 646 insufficient mechanical properties. Progress has been made in optimizing the process parameters,  
 647 methods, and the use of coating and interlayers. However, controlling the formation and  
 648 distribution of intermetallic compounds is a major barrier to overcome. Other welds defects such  
 649 as porosities and cracks need to be addressed as well. Table 4 gives the summary of research  
 650 carried out on dissimilar laser welding of steel and aluminum.

651

652

Materials	Interlayer	Laser process	Joint type	Optimum laser parameters	Intermetallics	Max. average tensile strength	Ref. (year)
1.2 mm Dual-Ten 590 steel/1.6 mm A6022-O aluminium	-	Not reported	Lap joint (steel on top)	Power: 3 kW Spot radius: 30 mm Pure Cu backing block	Not reported	70 Mpa	[80] (2007)
0.77 mm Zinc-coated low carbon steel/6016 T4 aluminium	-	Nd:YAG	Lap joint (Al on top)	Power: 1.6 - 2 kW Speed: 2 - 2.4 m/min Inclination angle: 35° Beam focus: +10 and +11 mm	FeAl <sub>3</sub> - Fe <sub>2</sub> Al <sub>5</sub>	Above 200 N/mm	[74] (2007)
1.2 mm low carbon steel DC04/1 mm 6016-T4 aluminium	1 mm filler wire 4047 Al alloy (Al-12Si)	Nd:YAG	Lap joint (Al on top)	Power: 2 – 2.5 kW Inclination angle: 30°	Thin (< 2 μm) Fe-Al-Si intermetallics	190 N/mm	[93] (2008)
0.8 mm low carbon steel st14/2 mm 5754 aluminium	-	Nd:YAG (Pulse mode)	Lap joint (steel on top)	Peak power: 1.43 kW Pulse duration: 5 ms Overlapping factor: 80%	FeAl <sub>2</sub> – FeAl <sub>3</sub> - Fe <sub>2</sub> Al <sub>5</sub>	Not reported	[70] (2010)
0.8 mm JSC270CC steel/1.2 mm A6111-T4 aluminium	-	Nd: YAG (Continuous and pulse mode)	Lap joint (steel on top)	CW laser power: 390 W PW peak power: 2.61 kW Pulse frequency: 5 Hz Pulse width: 2 ms Speed: 0.06 m/min	IMC layer below 10 μm	128 Mpa	[82] (2010)

1 mm 201 Stainless steel/ 1 mm 5052 Al	0.1 mm Ni foil	CO <sub>2</sub>	Lap joint (steel on top)	Power: 1 kW-3kW Speed: 1 m/min – 3 m/min Beam focus: +0.2 mm	FeAl <sub>3</sub> and Al <sub>0.9</sub> Ni <sub>1.1</sub>	~ 160 N/mm	[88] (2012)
1.2 mm H220YD galvanized steel/1.15 mm 6016 aluminum	1.2 mm filler wire 4043 Al alloy (Al-5Si)	Fiber	Butt joint	Power: 2.3 kW – 2.6 kW Speed: 1 m/min Filler wire feeding speed: 2.22 m/min Beam focus: +5 mm	1.3µm to 13µm composed of α(τ <sub>5</sub> )- Al <sub>8</sub> Fe <sub>2</sub> Si, θ-Al <sub>13</sub> Fe <sub>4</sub> and ζ-Al <sub>2</sub> Fe	162 MPa	[95] (2013)
0.75 mm DP590 galvanized steel/1 mm 6061-T6 aluminum	-	Fiber	Lap joint (Steel on top)	Laser preheating power: 4 kW Laser welding power: 3 kW Speed: 100 mm/s	iron-rich IMCs (Fe <sub>3</sub> Al, FeAl) and the Al-rich IMCs (FeAl <sub>2</sub> , Fe <sub>2</sub> Al <sub>5</sub> )	~ 160 N/mm	[79] (2014)
1 mm DC04 steel/1 mm 6111-T4 aluminium	-	Fiber	Lap joint (steel on top)	Cu backing bar Power density: 2.75 E-3 MW/cm <sup>2</sup> Interaction time: 3 s Specific point energy: 10.95 KJ Standard deviation: 1.26 µm	FeAl <sub>3</sub> - Fe <sub>2</sub> Al <sub>5</sub>	130 MPa	[81] (2014)
0.8 mm hot- dip galvanized steel/1.5 mm A5052-H34 aluminum	70-110 µm diameter pure Al powder	Nd:YAG	Lap joint (Al on top)	Laser power: 2250 W Defocusing distance: 12 mm Welding speed: 1 m/min Beam incline: 30°	FeAl <sub>3</sub> - Fe <sub>2</sub> Al <sub>5</sub> Fe <sub>2</sub> Al <sub>5</sub> Zn <sub>0.4</sub>	Not reported	[87] (2015)

2.5 mm Q235 low-carbon steel/2.5 mm 6013 aluminium	1.2 mm Al alloy (ER4043)	Fiber	Butt joint	Laser power: 3.05 kW Welding speed: 1.8 m/min Beam angle: 12° Beam focus: 2 mm above the surface	FeAl <sub>3</sub> - Fe <sub>2</sub> Al <sub>5</sub> – Al-Si eutectic	120 MPa	[92] (2015)
1 mm hot-dip 980 DP galvanized steel/2 mm 5754-O Al	1.6 mm filler wire 4047 Al alloy (Al-12Si)	Diode	Lap joint (Al on top)	Laser power: 2 kW Welding speed: 1 m/min Beam focus: 0 mm	$\theta$ -Fe(Al,Si) <sub>3</sub> and $\tau_5$ -Al <sub>7.2</sub> Fe <sub>1.8</sub> Si	~ 215 N/mm	[94] (2015)
1.2 mm DC56D +ZF steel/1.15 mm 6016 aluminium	0.02 mm pure Cu or Pb foil	CO <sub>2</sub>	Lap joint (steel on top)	Laser power: 1600 W Welding speed: 1100 mm/min Beam focus: -0.5 ± 1.0 mm	Al <sub>0.4</sub> Fe <sub>0.6</sub> , Mg <sub>2</sub> Zn <sub>11</sub> Mg <sub>2</sub> Pb	73.51 MPa	[89] (2016)
1 mm low carbon steel Q235/1 mm 5052 aluminum	0.1 mm Cu foil	CO <sub>2</sub>	Lap joint (steel on top)	Laser power: 2.5 kW dual-beam 1.6 kW single-beam Welding speed: 0.9-1.25 m/min dual-beam and 1.5-1.75 m/min single-beam	The Fe-Al interface: $\alpha$ -Al and Al <sub>2</sub> Cu eutectic structure, FeAl, FeAl <sub>2</sub> , a certain amount of Al-Cu intermetallics, Fe <sub>2</sub> Al <sub>5</sub> , and FeAl <sub>3</sub> . The Al-Cu interface: the eutectic phase Al <sub>2</sub> Cu and metastable phase of Al-Cu intermetallics.	74 N/mm dual-phase 65 N/mm single-phase	[46] (2016)

0.8 mm 316L stainless steel/0.8 mm 1060 pure aluminum	-	Nd:YAG (Pulse mode)	Lap joint (steel on top)	Laser mean power: 285 W Welding speed: 4 mm/s Beam focus: -0.6 mm	Fe- rich IMCs	46.2 ± 1.9 N/mm	[76] (2016)
1.4 mm DC56D + ZF steel/1.2 mm 6016 aluminium	75 µm pure Mn, Zr, or Sn powder	Fiber	Lap joint (steel on top)	Welding power: 1800-2000 W Welding speed: 45-50 mm/s Focus beam: +2 mm	FeAl, FeSn, FeAl <sub>3</sub>	62.17 MPa	[90] (2016)
2.5 mm DP600 steel/3 mm 6061 aluminium	-	Fiber-coupled diode	Lap joint (steel on top)	Laser power: 4 kW Scanning speed: 5 mm/s Pulse duration: 10 ms	FeAl <sub>3</sub> - Fe <sub>2</sub> Al <sub>5</sub>	Not reported	[75] (2018)
1.2 mm DP590 dual-phase steel/1.5 mm 6061-T6 aluminium	1.6 pure Al-1100, AlSi <sub>5</sub> -4043, and AlSi <sub>12</sub> -4047	Fiber	Butt joint	Laser power: 2 kW Welding speed: 0.5 m/min Laser offset: 0.4 mm towards Al Focus distance: +20 mm	τ <sub>5</sub> - Fe <sub>2</sub> Al <sub>8</sub> Si, θ-Fe(Al,Si) <sub>3</sub>	208 MPa	[96] (2018)
1 mm DP980 steel/1.5 mm 5754 aluminium	1.6 mm Al-1100, AlSi <sub>12</sub> , ZnAl <sub>22</sub>	Diode	Lap joint (steel on top)	Laser power: 1.0-2.8 kW Welding speed: 0.2-1.0 m/min Laser offset: 0 mm Focus distance: 0 mm	Si interlayer: Al <sub>7.2</sub> Fe <sub>1.8</sub> Si and Fe(Al,Si) <sub>3</sub> Zn-Al interlayer: Fe <sub>2</sub> Al <sub>5-x</sub> Zn <sub>x</sub> , FeZn <sub>10</sub> , and a small amount of Al-rich amorphous phase	1233 N	[91] (2018)



1.3 mm press-hardened steel/2 mm 5052 aluminum	0.05 mm and 0.1 mm brass	Fiber	Butt joint	Laser power: 1.2 kW Laser offset: 0.2 mm towards steel Welding speed: 12 mm/s	Fe <sub>3</sub> Al - Fe <sub>2</sub> Al <sub>5</sub> - FeAl	56.4 MPa	[71] (2019)
1 mm low carbon DC04/1 mm 6016 aluminum	-	Fiber	Lap joint (steel on top)	Laser power: 1400 W Welding speed: 40 mm/s Beam focus: 0 mm	FeAl <sub>3</sub> - Fe <sub>2</sub> Al <sub>5</sub>	Not reported	[78] (2019)
1 mm DP1000 steel/1 mm 1050 aluminium	-	Nd:YAG (Pulse mode)	Lap joint (steel on top)	Laser power: 6.48 kW Pulse duration: 14 ms	Not reported	120 MPa	[77] (2019)
1 mm DP590 galvanized steel/1 mm 6061-T6 aluminum	-	Fiber	Lap joint (steel on top)	Laser power: 3 kW Welding speed: 5 m/min Focus distance: +2 mm	Fe <sub>2</sub> Al <sub>5</sub> , FeAl <sub>3</sub> , Al <sub>192.4</sub> Fe <sub>46.22</sub> phase and a limited amount of FeAl and Fe <sub>3</sub> Al	1.22 kN	[83] (2019)

655

#### 656 4 Aluminum-copper

657 The aluminum and copper welds are of particular interest due to their low weight, cost  
658 efficiency, and electrical conductivity similar to that of copper alloys [97]. The phase diagram of  
659 Al-Cu is shown in Fig. 28. Similar to aluminum to steel welding, brittle intermetallic compounds  
660 are also formed during aluminum to copper welding causing crack sensitivity and poor mechanical  
661 properties. The intermetallic thickness larger than 5µm in these welds makes it highly brittle [98].  
662 Properties of the four main intermetallics between Al and Cu are presented in Table 5.

663

664

665

666

667

668

669

670

671

672

673

674

675

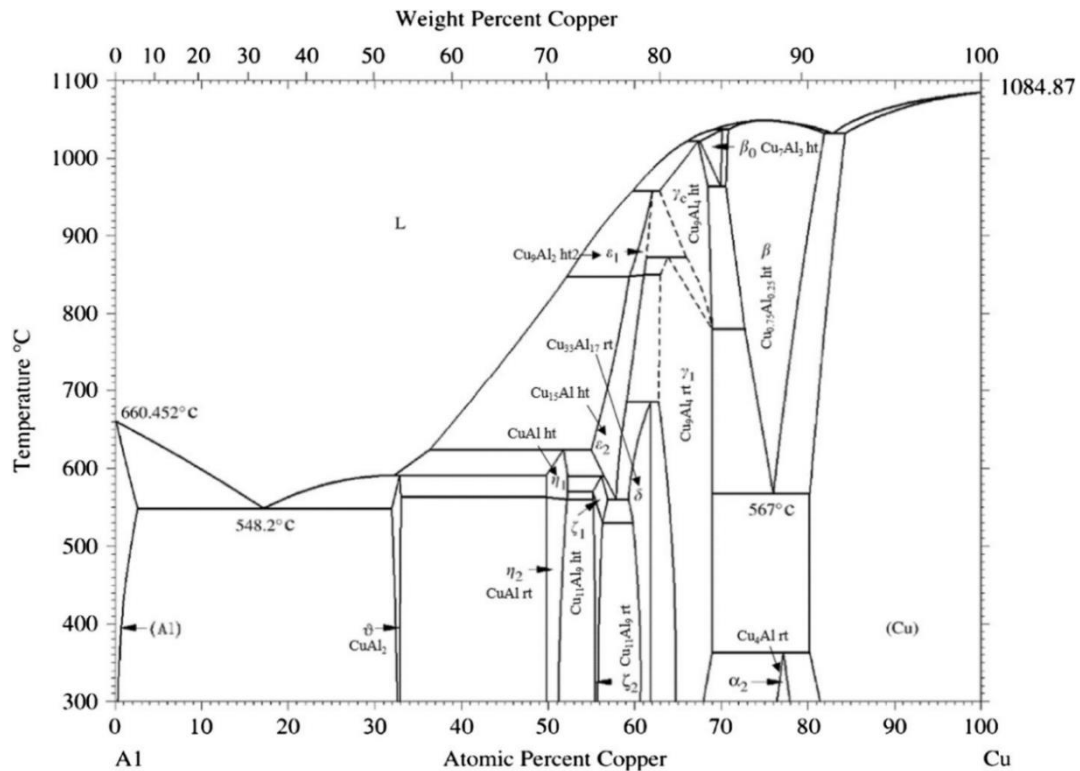


Fig. 28. Equilibrium phase diagram of Fe-Al system [99].

676

677

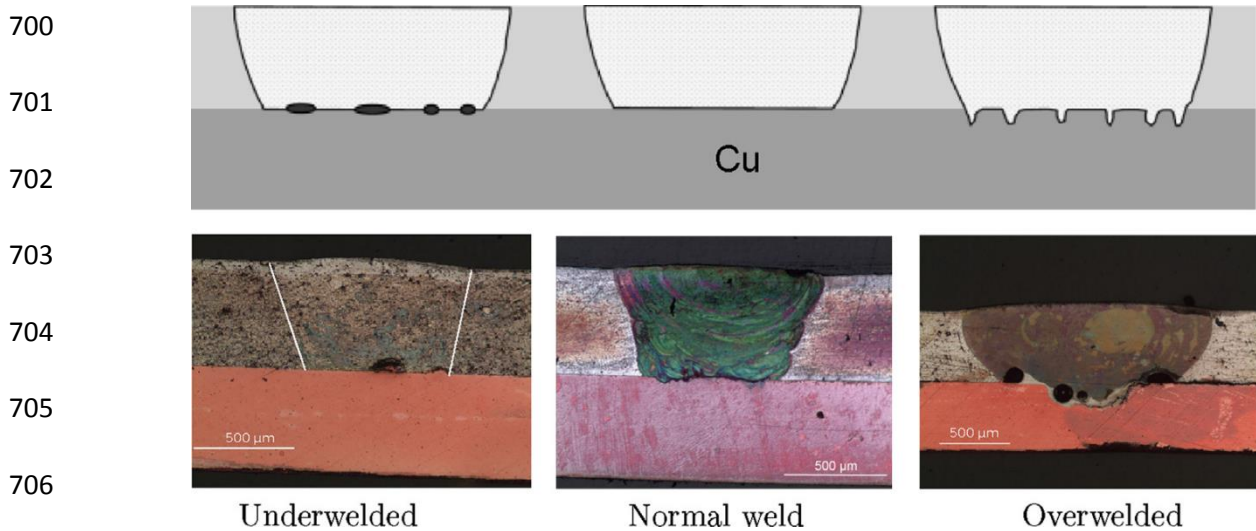
678 Table 5

679 Properties of important intermetallics between Al and Cu [100].

Phase	Cu content (at.%)	Structure	Microhardness (HV)	Density (g/cm <sup>3</sup> )	Specific resistance (μΩ cm)
CuAl <sub>2</sub>	33	Body-centered tetragonal	630	4.34	8
CuAl	51	Body-centered orthorhombic	905	5.13	11.4
Cu <sub>4</sub> Al <sub>3</sub>	55.5	Monoclinic	930	NA	12.2
Cu <sub>9</sub> Al <sub>4</sub>	66	Body—centered cubic	770	6.43	14.2

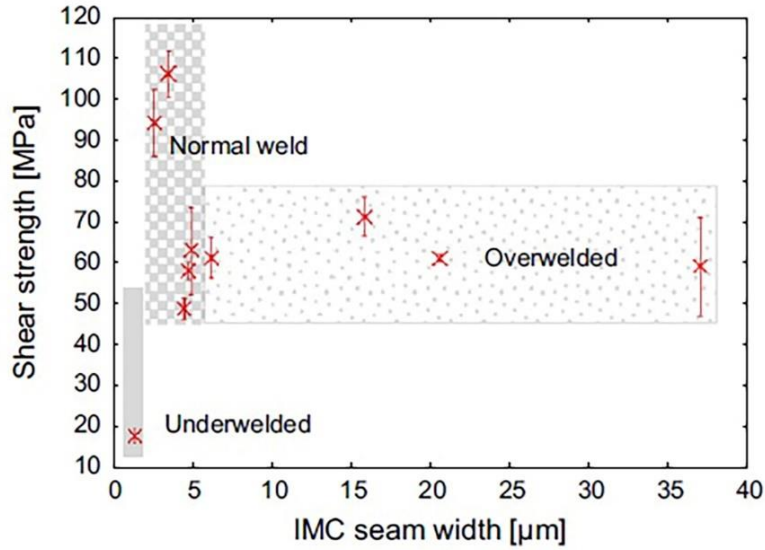
680 Solchencach et al. [101] studied the laser welding-brazing of 500μm thickness SF-Cu and the  
 681 aluminum alloy AA1050 in an overlap configuration. The laser beam melted the aluminum at the  
 682 top, which wetted the Cu surface thereby starting the diffusion process. They reported three  
 683 different seam structures with varied process parameters as shown in Fig. 29. The low energy input

684 led to the formation of voids and the “under-welded” joint. On the other hand, too much energy  
 685 input melted the copper sheet and created an “over-welded” joint with voids inside solidified  
 686 aluminum. The formation of aluminum-rich intermetallic ( $\text{Al}_2\text{Cu}$ ) with dendritic microstructure  
 687 was observed near aluminum, while a highly brittle intermetallic ( $\text{Al}_3\text{Cu}_4$ ) was present near copper.  
 688 The effect of intermetallic thickness on the shear strength for different seam welds is shown in Fig.  
 689 30. The weld with a homogenous interface structure and an intermetallic interlayer thickness of  
 690  $3.2\mu\text{m}$  had higher strength up to 105 MPa. The over-welded seams illustrated better shear strength  
 691 than under-welding, potentially due to mechanical interlocking at the over-welded regions.  
 692 Solchencach et al. [25] investigated the relationship between shear strength and the electrical  
 693 resistance in Al-Cu weld joints. They reported an inverse relationship as shown in Fig. 31. Four  
 694 modulation times of  $32\mu\text{s}$ ,  $42\mu\text{s}$ ,  $52\mu\text{s}$ , and  $62\mu\text{s}$  were compared. The lowest electrical  
 695 resistance was achieved for the welds exhibiting the highest shear strength ( $32\mu\text{s}$ ) and containing  
 696 the intermetallic layer with a thickness of  $3.2\mu\text{m}$ . An increase in joint electrical resistance was  
 697 detected for thicker intermetallic compounds. Similar results have been reported by Braunovic et  
 698 al. [102] indicating a linear increase in contact resistance with the thickness of intermetallic  
 699 compounds.



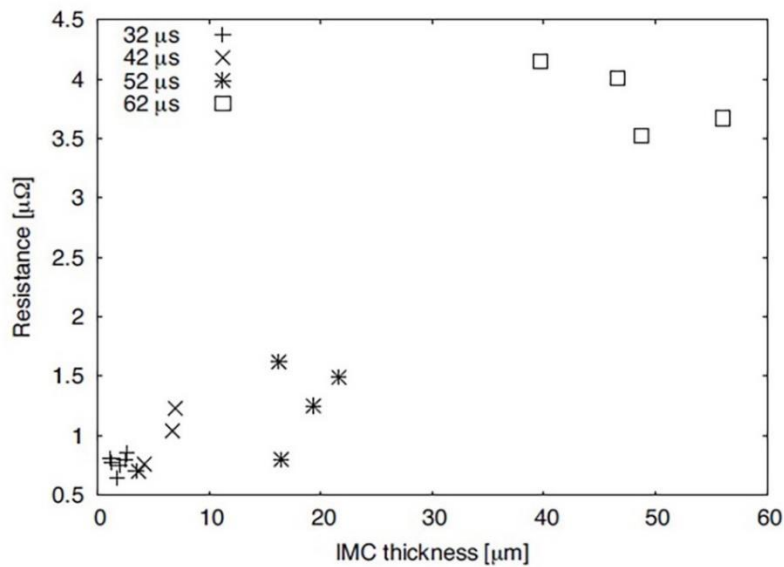
707 Fig. 29. Three different weld seam structures corresponding with welding conditions [101].

708  
709  
710  
711  
712  
713  
714  
715



716 Fig. 30. Correlation between intermetallic layer thickness and shear strength in joints with  
717 different welding seams [101].

718  
719  
720  
721  
722  
723  
724  
725

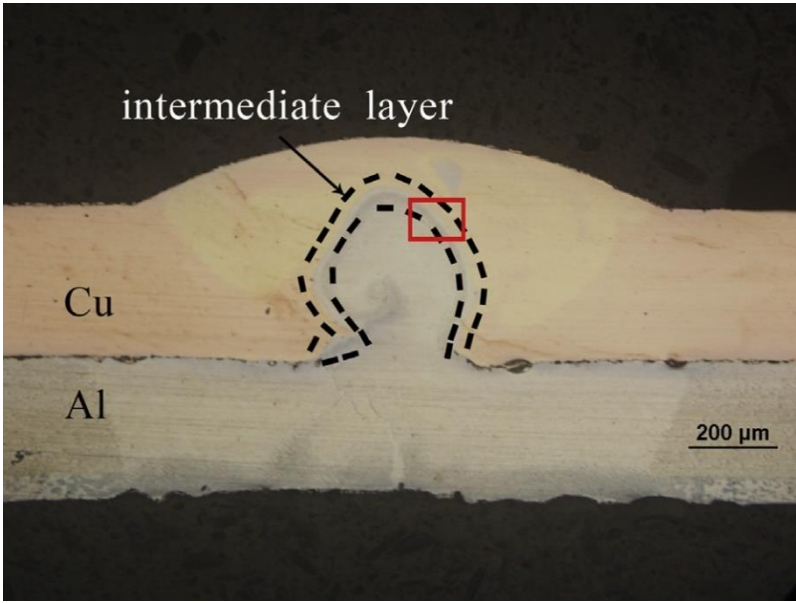


726 Fig. 31. The correlation between the intermetallic thickness and interface resistance [25].

727 Lee et al. [99] compared the overlap laser welding of aluminum and copper with aluminum at the  
728 top, as well as at the bottom. While using aluminum at the top, aluminum was floating on the Cu.  
729 However, for aluminum at the bottom, Cu could easily sink into the aluminum. As fluid flow was  
730 different for both weld configurations, this influenced the formation of intermetallics. For  
731 aluminum at the top, the formation of around 5 μm thickness AlCu<sub>2</sub> was observed, close to the

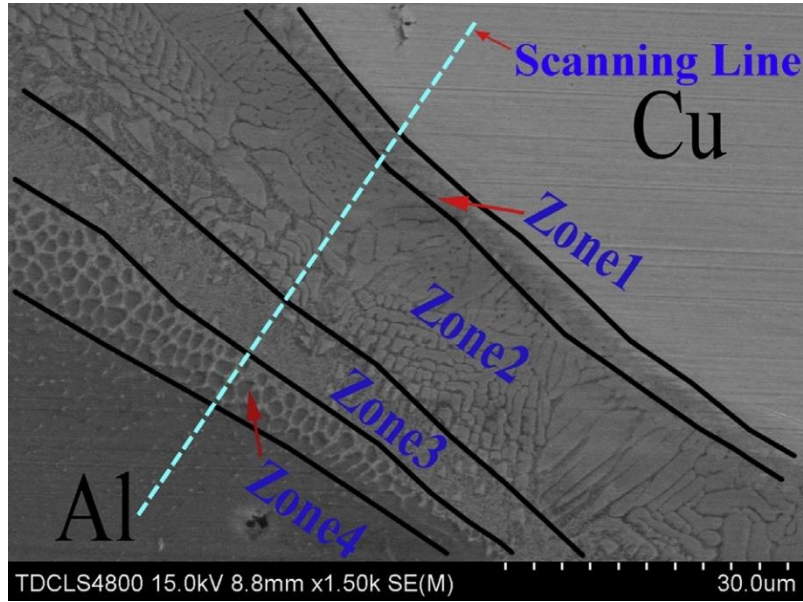
732 interface region. However, for aluminum at the bottom, a relatively large amount of  $\text{CuAl}_2$  and  
733  $\text{Cu}_9\text{Al}_4$  intermetallics were observed. The aluminum and the Cu solid solution were also formed  
734 on respective sides for both configurations. The effect of welding speed on the weld quality was  
735 also reported. The presence of  $\text{CuAl}_2$ ,  $\text{Cu}_9\text{Al}_4$ , and  $\text{CuAl}$  intermetallics was observed inside the  
736 weld region for a welding speed of 10 m/min. However, at the higher welding speed of 50 m/min,  
737 the formation of intermetallics was suppressed. In addition, the tensile strength improved with  
738 increasing welding speed, reaching 160 MPa for aluminum at the top and 205 MPa for aluminum  
739 at the bottom, for the welding speed of 50 m/min. In all samples, the fracture occurred in the  
740 intermetallic compound near the fusion zone interface. The fracture behavior and intermetallic  
741 formation in laser-welded samples of copper to aluminum were investigated by Zuo et al. [103].  
742 Fig. 32 shows the weld cross-section micrograph. Owing to the higher expansion coefficient of  
743 aluminum, an upward convexity of liquid aluminum was created. Since there is not sufficient time  
744 during solidification for the joint to get back to its original structure, the upward convexity resulted  
745 in a shallow weld pool and little mixing of two base metals. The four distinct zones that form the  
746 welding interlayer are shown in Fig. 33. Table 6 presents the composition and phase distribution  
747 of these ones.

748  
749  
750  
751  
752  
753  
754  
755



756 Fig. 32. Micrograph of weld cross-section with a laser power of 1650 W and a welding speed of  
757 95 mm/s [103].

758  
759  
760  
761  
762  
763  
764  
765



766 Fig. 33. Morphology of four distinct zones in the intermediate layer [103].

767

768 Table 6

769 Chemical composition of phases observed in Fig. 33 [103].

Zone	Concentration (wt% Cu)	Phase
1	62.18-64.45	Columnar grain ( $\gamma_2$ -Cu <sub>9</sub> Al <sub>4</sub> )
2	45.34-51.95 (white) 30.12-41.19 (gray)	Lump ( $\theta$ -CuAl <sub>2</sub> ) + eutectic ( $\alpha$ -Al + $\theta$ -CuAl <sub>2</sub> )
3	30.27-36.61	Eutectic ( $\alpha$ + $\theta$ )
4	≤8.55	Dendrites ( $\alpha$ -Al)

770 The first zone, adjacent to the Cu consisted of Cu<sub>9</sub>Al<sub>4</sub> columnar grains. This was the thinnest and  
771 most uniform region. The second zone was a mixture of a net-like eutectic  $\alpha$ -Al +  $\theta$ -CuAl<sub>2</sub> (gray  
772 area) and  $\theta$ -CuAl<sub>2</sub> (white area) structure. The concentration of CuAl<sub>2</sub> was higher on the Cu side,  
773 however, when moved away the CuAl<sub>2</sub> concentration decreased. Zone 3 contained the eutectic  
774 phase similar to zone 2, but finer in size and with an interlamellar spacing of less than 1  $\mu$ m. In  
775 zone 4, the growth of the solidification front and the segregation of alloying elements created the

776 dendrite microstructure. It was found that the presence of a thin, continuous, and uniform  $\gamma_2$ -  
777  $\text{Cu}_9\text{Al}_4$  phase improved the shear strength. In contrast, the brittle  $\theta$ - $\text{CuAl}_2$  phase had a detrimental  
778 effect on the weld strength, and the fracture that occurred in this zone illustrated a weaker cohesion  
779 in the aluminum side.

780 The application of sinusoidal beam oscillation was studied by Fetzer et al. [104] in overlap laser  
781 welding of oxygen-free copper and high-purity aluminum. By using suitable oscillation  
782 parameters, the weld composition could be managed. In the case of the smaller amplitude of 0.25  
783 mm the weld composition was very inhomogeneous and large cracks were seen. However, the  
784 larger amplitude of 0.75 mm decreased the amount of copper in the weld zone and fused copper  
785 was also distributed more homogeneously. No cracks were seen in this case. Circular laser beam  
786 oscillation was applied by Dimatteo et al. [28] in laser welding of Al and Cu sheets. Low electrical  
787 contact resistance and good mechanical properties were achieved with double weld seams. Lerra  
788 et al. [105] focused on pulse shape and separation distance in Nd:YAG laser welding of Al and  
789 Cu. With the process optimization a low penetrating depth with a maximum tensile load of over  
790 110 kgf was achieved. They also reported that preheating resulted in better mechanical properties  
791 and electrical resistance.

792 A number of studies have been carried out to appropriately select a filler alloy to minimize  
793 defects and improve mechanical properties in the Al-Cu joint. The effect of tin interlayer in laser  
794 welding of Al 3003-H14 and Cu110-H00 was studied by Hailat et al. [106]. Fig. 34 shows the Al-  
795 Cu weld cross-section with and without tin interlayer. Large porosities can be seen in aluminum  
796 in the weld with Sn interlayer. However, the fracture occurred away from these porosities therefore  
797 they did not affect the joint strength. Welds with tin filler metal exhibited a better lap shear strength  
798 possibly due to the formation of  $\text{Cu}_6\text{Sn}_5$  and  $\text{Cu}_3\text{Sn}$ . Mys and Schmidt [107] declared that while  
799 Ni resulted in only a slight improvement in the tensile strength, Ag and Sn foils considerably  
800 improved the tensile strength. The samples welded without silver interlayer showed a very small  
801 recrystallization zone on the copper side following by hard and brittle Cu-Al intermetallics.  
802 However, the joint produced with Ag exhibited a uniform distribution of Ag atoms in the silver-  
803 rich matrix. The high concentration of silver resulted in reasonable ductility and fatigue property.  
804 Similar results confirming the influence of Ag on the joint strength have been reported by Esser et  
805 al. [108].

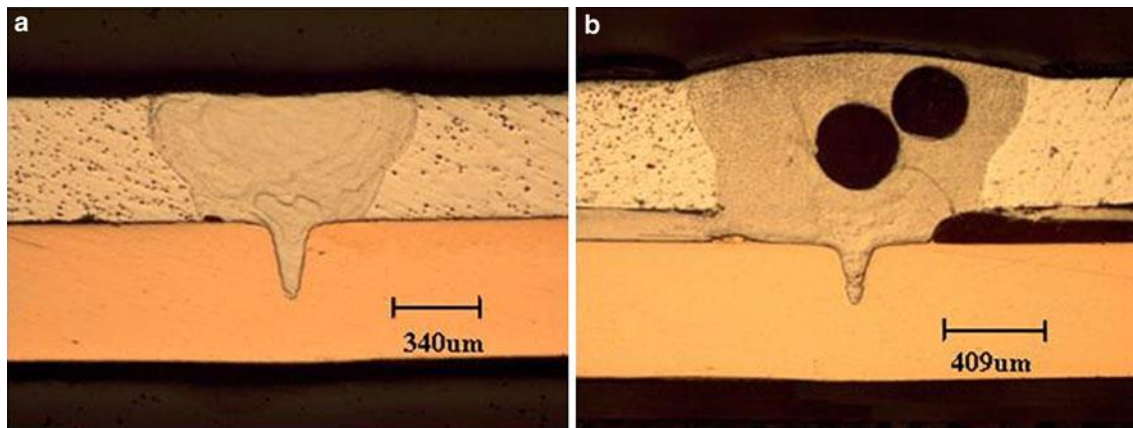


Fig. 34. Al-Cu laser weld (a) without Sn filler metal (b) with Sn filler metal [106].

806

807 The laser beam offset is recommended to restrict the growth of intermetallics in butt laser  
 808 welding of aluminum and copper, quite similar to the proposed earlier for butt welding of steel to  
 809 Cu. Mai and Spowage [45] investigated the laser welding of Cu and aluminum alloy AA4047 in  
 810 the butt configuration. The laser beam offset of 0.2 mm towards aluminum produced crack-free  
 811 welds with an elemental concentration of 48.4% Al, 24.3% Si, and 27.2% Cu. The weld nugget  
 812 had a very high hardness compared to the parent materials that was attributed to the supersaturated  
 813 solid solution or the formation of GP-zones. However, the increase in welding speed to more than  
 814 100 mm/min led to the solidification cracking at the weld joint.  $AlSi_{12}$  was used as filler materials  
 815 for laser welding of pure aluminum and copper by Weigl and Schmidt [109]. Both  $AlSi_{12}$  and  $CuSi_3$   
 816 enhanced the ductility of the joints and reduced the absolute value and fluctuation of  
 817 microhardness. However, the best results were achieved with  $AlSi_{12}$  owing to its higher percentage  
 818 of Si. It reduced the viscosity and enhanced the turbulence of the molten metal thereby improving  
 819 the element mixture in the weld zone.

820 Similar to laser welding of steel and aluminum optimization of the welding parameters, and the  
 821 use of coating and filler metals has been the subject of several investigations. However, the effect  
 822 of many potential interlayers on the formation of new intermetallics needs further studies. Table 7  
 823 gives a summary of the research conducted on laser welding of aluminum and copper thus far.

824

825

826



Materials	Interlayer	Laser process	Joint type	Optimum laser parameters	Intermetallics	Max. average tensile strength	Ref. (year)
1 mm copper/ 1 mm 4047 Al	-	Nd:YAG (Pulse mode)	Butt joint	Power: 275 W Speed: 75 mm/min Pulse frequency: 15 Hz Pulse width: 8 ms	Not reported	Not reported	[45] (2004)
1.2 mm Cu/1.2 mm Al	0.1 mm Ag 0.1 mm Ni	Nd:YAG (Pulse mode)	Lap joint (Cu on top)	Laser power: 3kW Beam offset: 0.1 mm towards Al	Not reported	800 N	[108] (2004)
1.2 mm Cu/1.2 mm Al	0.1 mm Ag	Nd:YAG (Pulse mode)	Lap joint (Al on top)	Laser power: 3kW Beam offset: 0.1-0.2 mm towards Al	Not reported	800 N	[107] (2006)
1 mm Cu/1 mm Al	1.6 mm filler wire AlSi <sub>12</sub>	Pulse mode	Butt joint	Laser power: 200 W	Not reported	Not reported	[109] (2011)
0.54 mm 110-H00 copper/0.49 mm 3003-H14	100 μm tin	Fiber	Lap joint (Al on top)	Laser power: 460 W Welding speed: 1 m/min Beam incline: 15°	Not reported	780 N	[106] (2012)
0.5 mm SF-Cu copper/0.5 mm AW1050A	-	Fiber	Lap joint (Al on top)	Laser power: 400 W Beam focus: 1 mm below the surface	Al <sub>2</sub> Cu – Al <sub>4</sub> Cu <sub>9</sub>	121 MPa	[101] (2013)

0.3 mm Copper /0.3 mm Aluminium A1050	-	Fiber	Lap joint	Laser power: 1 kW Welding speed: 50 m/min	CuAl <sub>2</sub> – Cu <sub>9</sub> Al <sub>4</sub> - CuAl	205 Mpa	[99] (2014)
0.3 mm T2 Copper/0.3 mm Aluminum A1060	-	Nd:YAG	Lap joint (Cu on top)	Laser power: 1.65 kW Welding speed: 95 mm/s	CuAl <sub>2</sub> – Cu <sub>9</sub> Al <sub>4</sub>	539.52 N	[103] (2014)
1 mm Cu/1 mm Al	-	Fiber	Lap joint (Al on top)	Laser power: 3.25 kW Feed rate: 6 m/min Beam incline: 10°	Not reported	Not reported	[104] (2016)
0.3 mm C1020-HO Copper/0.45 mm Aluminum A1050	2.5 μm electroplated Ni layer on Cu	Fiber	Lap joint (Cu on top)	Laser power: 800 W Welding speed: 134 mm/s Wobbling amplitude: 0.7 mm	Not reported	120 kgf	[28] (2019)
0.3 mm C1020-HO Copper/0.45 mm Aluminum A1050	2.5 μm electroplated Ni layer on Cu	Nd:YAG (Pulse mode)	Lap joint (Al on top)	Laser power: 6 kW Pulse energy: 13 J Pulse separation distance: 0.1-0.32 mm	Not reported	110 kgf	[105] (2019)

829

#### 830 4 Steel-nickel

831 Steel-nickel dissimilar joint is another potential combination of battery tab and busbar in EV  
832 battery pack. Hu et al. [110] developed a three-dimensional transient numerical model for heat and

833 mass transfer to calculate weld geometry and element distribution in laser spot welding of 304  
 834 stainless steel and nickel. They observed that elements were uniformly distributed in the weld pool  
 835 which agreed well with calculated results. Porosity formation in laser welding of pure nickel and  
 836 martensitic stainless steel was studied by Zhang et al. [111]. They concluded that shielding gas has  
 837 no effect on porosity formation, but there was a direct relationship between the pulse width and  
 838 porosity number. When the pulse width was less than 5 ms the porosity was completely suppressed  
 839 resulting in a better joint. Li et al. [112] investigated the effect of different heat inputs in laser  
 840 welding of 304 stainless steel and Ni. The cooling rate was highly dependent on the heat input  
 841 affecting the grain dimension.

842 The information regarding the dissimilar laser welding of steel and nickel is very limited and  
 843 the metallurgical aspects of this joint has not been much explored yet. The summary of the research  
 844 conducted on laser welding of steel and nickel is presented in Table 8.

845

846 Table 8

847 Summary of research conducted on laser beam welding of steel and nickel

Materials	Laser process	Joint type	Optimum laser parameters	Weld characteristics	Ref. (year)
2 mm nickel/2 mm 304 stainless steel	Nd: YAG	Butt joint	Laser power: 650 W	Uniform distribution of element Fe in the weld pool	[110] (2012)
0.3 ~ 0.5 mm pure nickel/stainless steel SUS440C	Fiber	Lap joint (Ni on top)	Welding speed: 4.7 mm/s Beam spot size: 0.1mm Laser peak power: 300 W	Complete elimination of porosities	[111] (2013)
2 mm nickel/2 mm 304 stainless steel	Nd: YAG	Butt joint	Laser power: 800 W Laser speed: 10-30 mm/s Laser spot: 0.57 mm	Nearly defect-free joints	[112] (2018)

848

## 849 5 Summary and outlook

850 Laser welding is a robust and contact-free welding process with high control of energy  
851 deposition which provides a crucial way for joining temperature-sensitive and dissimilar material  
852 components such as battery cells in the EV battery system. Laser welding of dissimilar materials  
853 has continued to develop over the past two decades. However, despite several studies on different  
854 laser sources, optimization of process parameters, and various joint configurations, metallurgical  
855 defects such as incomplete bonding, brittle intermetallic phases, corrosion, excessive porosities,  
856 and cracking have persisted. These defects greatly undermine the mechanical and electrical  
857 performance of EV battery joints. Thus, further investigation is needed before laser welding can  
858 be widely used for EV battery manufacturing.

859 In this review paper, the research on the laser welding process for joining the different  
860 combinations of dissimilar materials including steel-copper, steel-aluminum, aluminum-copper,  
861 and steel-nickel was summarized. Based on the studies so far, some suggestions for future research  
862 in this field are as follows:

- 863 (1) The precise control of heat input through the optimization of process parameters can  
864 improve the weld quality by controlling the thickness of IMCs. However, owing to the low  
865 thickness of materials involved in EV battery further investigations are needed to determine  
866 the optimum welding parameters such as welding speed and beam oscillation frequency  
867 for each weld combination and configuration.
- 868 (2) The use of appropriate interlayer materials and coatings can tailor the microscopic structure  
869 through modification of IMC composition which can improve mechanical performance and  
870 reduce electrical resistance. The applicability of many potential interlayers especially when  
871 there is a higher possibility for intermetallic formation has not been explored yet.
- 872 (3) Industrial lasers in infrared wavelength (1064 nm) have typically been used thus far for  
873 joining dissimilar materials in keyhole mode. Novel lasers with lower wavelengths and  
874 higher power including blue laser (wavelength ~ 450 nm) and green laser (wavelength ~  
875 515 nm) have been introduced in recent years with much higher energy absorption on  
876 highly reflective materials such as copper and aluminum. However, these laser systems  
877 still have not been explored for dissimilar welding in EV battery manufacturing.

- 878 (4) There have hardly been any reports on the evolution of intermetallic phases during the  
879 battery's long-term service. To guarantee the reliability of dissimilar joints, the effects of  
880 various thermal conditions on the intermetallic formation and thickness should be  
881 investigated.
- 882 (5) Most of the studies so far have been conducted on the static mechanical properties of laser-  
883 welded dissimilar joints, while hardly any data is available on fatigue behavior despite its  
884 importance in predicting the structural performance under cyclic loading.
- 885 (6) While there has been limited work on the electrical performance of dissimilar joints in EV  
886 battery, the electrical resistivity of joints or "connection resistance" has not been fully  
887 explored. The high resistance leads to energy loss and heat generation at the weld interface  
888 during the charging and discharging. Therefore, future studies and standardization of  
889 measurement methods are needed in the area.
- 890 (7) Some progress has been achieved in studying the corrosion performance of laser-welded  
891 joints especially about galvanic corrosion of steel/aluminum couple. However, the  
892 relationship between corrosion and mechanical properties in laser welding of EV battery  
893 materials requires further investigation.

894

895

## References

- 896 1. Iea I (2012) CO2 emissions from fuel combustion highlights. International Energy Agency  
897 Paris,
- 898 2. Hao H, Geng Y, Sarkis J (2016) Carbon footprint of global passenger cars: Scenarios through  
899 2050. *Energy* 101:121-131
- 900 3. Eskander SMSU, Fankhauser S (2020) Reduction in greenhouse gas emissions from national  
901 climate legislation. *Nature Climate Change* 10 (8):750-756
- 902 4. Wimbadi RW, Djalante R (2020) From decarbonization to low carbon development and  
903 transition: A systematic literature review of the conceptualization of moving toward net-zero  
904 carbon dioxide emission (1995–2019). *Journal of Cleaner Production* 256:120307
- 905 5. Pereirinha PG, González M, Carrilero I, Anseán D, Alonso J, Viera JC (2018) Main trends and  
906 challenges in road transportation electrification. *Transportation research procedia* 33:235-242

- 907 6. Salvia M, Reckien D, Pietrapertosa F, Eckersley P, Spyridaki N-A, Krook-Riekkola A, Olazabal  
908 M, Hurtado SDG, Simoes SG, Geneletti D (2021) Will climate mitigation ambitions lead to carbon  
909 neutrality? An analysis of the local-level plans of 327 cities in the EU. *Renewable and Sustainable*  
910 *Energy Reviews* 135:110253
- 911 7. Schreyer F, Luderer G, Rodrigues R, Pietzcker RC, Baumstark L, Sugiyama M, Brecha RJ,  
912 Ueckerdt F (2020) Common but differentiated leadership: strategies and challenges for carbon  
913 neutrality by 2050 across industrialized economies. *Environmental Research Letters* 15  
914 (11):114016
- 915 8. Yang M, Yang F (2020) Net zero-carbon energy in rural China. *Frontiers Journal of Renewable*  
916 *Energy* 1 (1):1-24
- 917 9. IEA (2020), *Global EV Outlook 2020*, IEA, Paris [https://www.iea.org/reports/global-ev-](https://www.iea.org/reports/global-ev-outlook-2020)  
918 [outlook-2020](https://www.iea.org/reports/global-ev-outlook-2020).
- 919 10. Das A, Barai A, Masters I, Williams D (2019) Comparison of tab-to-busbar ultrasonic joints  
920 for electric vehicle Li-ion battery applications. *World Electric Vehicle Journal* 10 (3):55
- 921 11. Giansoldati M, Monte A, Scorrano M (2020) Barriers to the adoption of electric cars: Evidence  
922 from an Italian survey. *Energy Policy* 146:111812
- 923 12. Xu M, Yang H, Wang S (2020) Mitigate the range anxiety: Siting battery charging stations for  
924 electric vehicle drivers. *Transportation Research Part C: Emerging Technologies* 114:164-188
- 925 13. Zhang J, Tang T-Q, Yan Y, Qu X (2021) Eco-driving control for connected and automated  
926 electric vehicles at signalized intersections with wireless charging. *Applied Energy* 282:116215
- 927 14. Eisel M, Nastjuk I, Kolbe LM (2016) Understanding the influence of in-vehicle information  
928 systems on range stress—Insights from an electric vehicle field experiment. *Transportation research*  
929 *part F: traffic psychology and behaviour* 43:199-211
- 930 15. Varga BO, Sagoian A, Mariasiu F (2019) Prediction of electric vehicle range: A comprehensive  
931 review of current issues and challenges. *Energies* 12 (5):946
- 932 16. Thorgeirsson AT, Vaillant M, Scheubner S, Gauterin F (2021) Evaluating system architectures  
933 for driving range estimation and charge planning for electric vehicles. *Software: Practice and*  
934 *Experience* 51 (1):72-90
- 935 17. Weil M, Ziemann S, Peters J (2018) The issue of metal resources in Li-ion batteries for electric  
936 vehicles. In: *Behaviour of lithium-ion batteries in electric vehicles*. Springer, pp 59-74

- 937 18. Zhang Q, Li C, Wu Y (2017) Analysis of research and development trend of the battery  
938 technology in electric vehicle with the perspective of patent. *Energy Procedia* 105:4274-4280
- 939 19. Deng J, Bae C, Denlinger A, Miller T (2020) Electric vehicles batteries: requirements and  
940 challenges. *Joule* 4 (3):511-515
- 941 20. Das A, Li D, Williams D, Greenwood D (2018) Joining technologies for automotive battery  
942 systems manufacturing. *World Electric Vehicle Journal* 9 (2):22
- 943 21. Zwicker MFR, Moghadam M, Zhang W, Nielsen CV (2020) Automotive battery pack  
944 manufacturing—a review of battery to tab joining. *Journal of Advanced Joining Processes* 1:100017
- 945 22. Cai W (2016) Lithium-Ion Battery Manufacturing For Electric Vehicles: A Contemporary  
946 Overview. *Advances in Battery Manufacturing, Service, and Management Systems* 1
- 947 23. Saariluoma H, Piironen A, Unt A, Hakanen J, Rautava T, Salminen A (2020) Overview of  
948 Optical Digital Measuring Challenges and Technologies in Laser Welded Components in EV  
949 Battery Module Design and Manufacturing. *Batteries* 6 (3):47
- 950 24. Taheri P, Hsieh S, Bahrami M (2011) Investigating electrical contact resistance losses in  
951 lithium-ion battery assemblies for hybrid and electric vehicles. *Journal of Power Sources* 196  
952 (15):6525-6533
- 953 25. Solchenbach T, Plapper P, Cai W (2014) Electrical performance of laser braze-welded  
954 aluminum–copper interconnects. *Journal of Manufacturing Processes* 16 (2):183-189
- 955 26. Trinh LN, Lee D (2020) The Characteristics of Laser Welding of a Thin Aluminum Tab and  
956 Steel Battery Case for Lithium-Ion Battery. *Metals* 10 (6):842
- 957 27. Wang P, Chen X, Pan Q, Madigan B, Long J (2016) Laser welding dissimilar materials of  
958 aluminum to steel: an overview. *The International Journal of Advanced Manufacturing*  
959 *Technology* 87 (9):3081-3090
- 960 28. Dimatteo V, Ascari A, Fortunato A (2019) Continuous laser welding with spatial beam  
961 oscillation of dissimilar thin sheet materials (Al-Cu and Cu-Al): Process optimization and  
962 characterization. *Journal of Manufacturing Processes* 44:158-165
- 963 29. Fleckenstein M, Bohlen O, Roscher MA, Bäker B (2011) Current density and state of charge  
964 inhomogeneities in Li-ion battery cells with LiFePO<sub>4</sub> as cathode material due to temperature  
965 gradients. *Journal of Power Sources* 196 (10):4769-4778

- 966 30. Qiu J (2006) Corrosion in Microelectronics. In: Cramer SD, Covino BS, Jr. (eds) Corrosion:  
967 Environments and Industries, vol 13C. ASM International, p 0.  
968 doi:10.31399/asm.hb.v13c.a0004170
- 969 31. Antler M (1999) Tribology of electronic connectors: Contact sliding wear, fretting, and  
970 lubrication. In: Electrical contacts. CRC Press, pp 337-408
- 971 32. Lee SS, Kim TH, Hu SJ, Cai W, Abell JA, Li J (2013) Characterization of ultrasonic metal  
972 weld quality for lithium-ion battery tab joining. *ASME J Manuf Sci Eng* 135 (2):021004
- 973 33. Shui L, Chen F, Garg A, Peng X, Bao N, Zhang J (2018) Design optimization of battery pack  
974 enclosure for electric vehicle. *Structural and Multidisciplinary Optimization* 58 (1):331-347
- 975 34. Brand MJ, Kolp EI, Berg P, Bach T, Schmidt P, Jossen A (2017) Electrical resistances of  
976 soldered battery cell connections. *Journal of Energy Storage* 12:45-54
- 977 35. Das A, Li D, Williams D, Greenwood D (2019) Weldability and shear strength feasibility study  
978 for automotive electric vehicle battery tab interconnects. *Journal of the Brazilian Society of*  
979 *Mechanical Sciences and Engineering* 41 (1):54
- 980 36. Mypati O, Mishra D, Sahu S, Pal SK, Srirangam P (2020) A Study on Electrical and  
981 Electrochemical Characteristics of Friction Stir Welded Lithium-Ion Battery Tabs for Electric  
982 Vehicles. *Journal of Electronic Materials* 49 (1):72-87
- 983 37. Pragana JPM, Baptista RJS, Bragança IMF, Silva CMA, Alves LM, Martins PAF (2020)  
984 Manufacturing hybrid busbars through joining by forming. *Journal of Materials Processing*  
985 *Technology* 279:116574
- 986 38. Zhang Q, Sekol RC, Zhang C, Li Y, Carlson BE (2019) Joining lithium-ion battery tabs using  
987 solder-reinforced adhesive. *Journal of Manufacturing Science and Engineering* 141 (4)
- 988 39. Dhara S, Das A (2020) Impact of ultrasonic welding on multi-layered Al–Cu joint for electric  
989 vehicle battery applications: A layer-wise microstructural analysis. *Materials Science and*  
990 *Engineering: A* 791:139795
- 991 40. Wu X, Liu T, Cai W (2015) Microstructure, welding mechanism, and failure of Al/Cu  
992 ultrasonic welds. *Journal of Manufacturing Processes* 20:321-331
- 993 41. Kundrat J, Alexy M Batteries need strong connections-are resistance, laser and micro TIG  
994 welding the best suited joining technologies? In, 2018 2018. pp 97-114



- 995 42. Lee SS, Kim TH, Hu SJ, Cai WW, Abell JA (2010) Joining technologies for automotive  
996 lithium-ion battery manufacturing: A review. In, 2010 2010. American Society of Mechanical  
997 Engineers Digital Collection, pp 541-549
- 998 43. Chen X, Wang X, Liu Z, Hu Z, Huan P, Yan Q, Hiromi N (2020) Effect of Cu content on  
999 microstructure transformation and mechanical properties of Fe-Al dissimilar laser welded joints.  
1000 Optics & Laser Technology 126:106078
- 1001 44. Brand MJ, Schmidt PA, Zaeh MF, Jossen A (2015) Welding techniques for battery cells and  
1002 resulting electrical contact resistances. Journal of Energy Storage 1:7-14
- 1003 45. Mai TA, Spowage AC (2004) Characterisation of dissimilar joints in laser welding of steel–  
1004 kovar, copper–steel and copper–aluminium. Materials Science and Engineering: A 374 (1-2):224-  
1005 233
- 1006 46. Chen S, Zhai Z, Huang J, Zhao X, Xiong J (2016) Interface microstructure and fracture  
1007 behavior of single/dual-beam laser welded steel-Al dissimilar joint produced with copper  
1008 interlayer. The International Journal of Advanced Manufacturing Technology 82 (1-4):631-643
- 1009 47. Das A, Fritz R, Finuf M, Masters I (2020) Blue laser welding of multi-layered AISI 316L  
1010 stainless steel micro-foils. Optics & Laser Technology 132:106498
- 1011 48. Haubold M, Ganser A, Eder T, Zäh MF (2018) Laser welding of copper using a high power  
1012 disc laser at green wavelength. Procedia CIRP 74:446-449
- 1013 49. Sun Z, Ion JC (1995) Laser welding of dissimilar metal combinations. Journal of Materials  
1014 Science 30 (17):4205-4214
- 1015 50. Shi RP, Wang CP, Wheeler D, Liu XJ, Wang Y (2013) Formation mechanisms of self-  
1016 organized core/shell and core/shell/corona microstructures in liquid droplets of immiscible alloys.  
1017 Acta materialia 61 (4):1229-1243
- 1018 51. Phanikumar G, Manjini S, Dutta P, Chattopadhyay K, Mazumder J (2005) Characterization of  
1019 a continuous CO<sub>2</sub> laser-welded Fe-Cu dissimilar couple. Metallurgical and Materials Transactions  
1020 A 36 (8):2137-2147
- 1021 52. Velu M, Bhat S (2013) Metallurgical and mechanical examinations of steel–copper joints arc  
1022 welded using bronze and nickel-base superalloy filler materials. Materials & Design 47:793-809
- 1023 53. Chen S, Huang J, Xia J, Zhang H, Zhao X (2013) Microstructural characteristics of a stainless  
1024 steel/copper dissimilar joint made by laser welding. Metallurgical and Materials Transactions A  
1025 44 (8):3690-3696

- 1026 54. Li Z, Fontana G, Penasa M (1998) Autogenous laser welding of austenitic stainless steel to  
1027 copper alloy. *Science and Technology of Welding and Joining* 3 (2):81-87
- 1028 55. Yao C, Xu B, Zhang X, Huang J, Fu J, Wu Y (2009) Interface microstructure and mechanical  
1029 properties of laser welding copper–steel dissimilar joint. *Optics and Lasers in Engineering* 47 (7-  
1030 8):807-814
- 1031 56. Chen S, Huang J, Xia J, Zhao X, Lin S (2015) Influence of processing parameters on the  
1032 characteristics of stainless steel/copper laser welding. *Journal of Materials Processing Technology*  
1033 222:43-51
- 1034 57. Li J, Cai Y, Yan F, Wang C, Zhu Z, Hu C (2020) Porosity and liquation cracking of dissimilar  
1035 Nd: YAG laser welding of SUS304 stainless steel to T2 copper. *Optics & Laser Technology*  
1036 122:105881
- 1037 58. Kuryntsev SV, Morushkin AE, Gilmudinov AK (2017) Fiber laser welding of austenitic steel  
1038 and commercially pure copper butt joint. *Optics and Lasers in Engineering* 90:101-109
- 1039 59. Moharana BR, Sahu SK, Maiti A, Sahoo SK, Moharana TK (2020) An experimental study on  
1040 joining of AISI 304 SS to Cu by Nd-YAG laser welding process. *Materials Today: Proceedings*
- 1041 60. Moharana BR, Sahu SK, Sahoo SK, Bathe R (2016) Experimental investigation on mechanical  
1042 and microstructural properties of AISI 304 to Cu joints by CO2 laser. *Engineering Science and*  
1043 *Technology, an International Journal* 19 (2):684-690
- 1044 61. Nguyen Q, Azadkhou A, Akbari M, Panjehpour A, Karimipour A (2020) Experimental  
1045 investigation of temperature field and fusion zone microstructure in dissimilar pulsed laser welding  
1046 of austenitic stainless steel and copper. *Journal of Manufacturing Processes* 56:206-215
- 1047 62. Ramachandran S, Lakshminarayanan AK (2020) An insight into microstructural  
1048 heterogeneities formation between weld subregions of laser welded copper to stainless steel joints.  
1049 *Transactions of Nonferrous Metals Society of China* 30 (3):727-745
- 1050 63. Shen H, Gupta MC (2004) Nd: yttrium–aluminum–garnet laser welding of copper to stainless  
1051 steel. *Journal of Laser Applications* 16 (1):2-8
- 1052 64. Sahul M, Tomčíková E, Sahul M, Pašák M, Ludrovcová B, Hodúlová E (2020) Effect of disk  
1053 laser beam offset on the microstructure and mechanical properties of copper—AISI 304 stainless  
1054 steel dissimilar metals joints. *Metals* 10 (10):1294
- 1055 65. Weigl M, Schmidt M (2010) Influence of the feed rate and the lateral beam displacement on  
1056 the joining quality of laser-welded copper-stainless steel connections. *Physics Procedia* 5:53-59

- 1057 66. Joshi GR, Badheka VJ (2019) Processing of bimetallic steel-copper joint by laser beam  
1058 welding. *Materials and Manufacturing Processes* 34 (11):1232-1242
- 1059 67. Mehlmann B, Olowinsky A, Thuilot M, Gillner A (2014) Spatially Modulated Laser Beam  
1060 Micro Welding of CuSn6 and Nickel-plated DC04 Steel for Battery Applications. *Journal of Laser*  
1061 *Micro/Nanoengineering* 9 (3)
- 1062 68. Iqbal N, Nath S, Coleman AE, Lawrence J Parametric Study of Pulse Arc Welding (PAW) and  
1063 Laser Beam Welding (LBW) Techniques for Electrical Vehicle Battery Cells. In, 2021. *Trans Tech*  
1064 *Publ*, pp 611-617
- 1065 69. Shaikh UF, Das A, Barai A, Masters I Electro-Thermo-Mechanical Behaviours of Laser Joints  
1066 for Electric Vehicle Battery Interconnects. In, 2019 2019. *IEEE*, pp 1-6
- 1067 70. Torkamany MJ, Tahamtan S, Sabbaghzadeh J (2010) Dissimilar welding of carbon steel to  
1068 5754 aluminum alloy by Nd: YAG pulsed laser. *Materials & Design* 31 (1):458-465
- 1069 71. Cao X, Zhou X, Li Z, Luo Z, Duan Ja (2019) Interface microstructure and nanoindentation  
1070 characterization of laser offset welded 5052 aluminum to press-hardened steel using a brass  
1071 interlayer. *Metals* 9 (11):1143
- 1072 72. Okamoto H, Massalski TB (1990) Binary alloy phase diagrams. ASM International, Materials  
1073 Park, OH, USA
- 1074 73. Tricarico L, Spina R, Sorgente D, Brandizzi M (2009) Effects of heat treatments on mechanical  
1075 properties of Fe/Al explosion-welded structural transition joints. *Materials & Design* 30 (7):2693-  
1076 2700
- 1077 74. Mathieu A, Shabadi R, Deschamps A, Suery M, Mattei S, Grevey D, Cicala E (2007)  
1078 Dissimilar material joining using laser (aluminum to steel using zinc-based filler wire). *Optics &*  
1079 *Laser Technology* 39 (3):652-661
- 1080 75. Indhu R, Divya S, Tak M, Soundarapandian S (2018) Microstructure development in pulsed  
1081 laser welding of dual phase steel to aluminium alloy. *Procedia Manufacturing* 26:495-502
- 1082 76. Jin Y, Li Y-l, Zhang H (2016) Microstructure and mechanical properties of pulsed laser welded  
1083 Al/steel dissimilar joint. *Transactions of Nonferrous Metals Society of China* 26 (4):994-1002
- 1084 77. Pereira AB, Cabrinha A, Rocha F, Marques P, Fernandes FAO, Alves de Sousa RJ (2019)  
1085 Dissimilar metals laser welding between DP1000 steel and aluminum alloy 1050. *Metals* 9 (1):102

- 1086 78. Guan Q, Long J, Yu P, Jiang S, Huang W, Zhou J (2019) Effect of steel to aluminum laser  
1087 welding parameters on mechanical properties of weld beads. *Optics & Laser Technology* 111:387-  
1088 394
- 1089 79. Ma J, Harooni M, Carlson B, Kovacevic R (2014) Dissimilar joining of galvanized high-  
1090 strength steel to aluminum alloy in a zero-gap lap joint configuration by two-pass laser welding.  
1091 *Materials & Design* 58:390-401
- 1092 80. Borrisutthekul R, Yachi T, Miyashita Y, Mutoh Y (2007) Suppression of intermetallic reaction  
1093 layer formation by controlling heat flow in dissimilar joining of steel and aluminum alloy.  
1094 *Materials Science and Engineering: A* 467 (1-2):108-113
- 1095 81. Pardal G, Meco S, Ganguly S, Williams S, Prangnell P (2014) Dissimilar metal laser spot  
1096 joining of steel to aluminium in conduction mode. *The International Journal of Advanced*  
1097 *Manufacturing Technology* 73 (1-4):365-373
- 1098 82. Yan S, Hong Z, Watanabe T, Jingguo T (2010) CW/PW dual-beam YAG laser welding of  
1099 steel/aluminum alloy sheets. *Optics and Lasers in Engineering* 48 (7-8):732-736
- 1100 83. Yan F, Wang X, Chai F, Ma H, Tian L, Du X, Wang C, Wang W (2019) Improvement of  
1101 microstructure and performance for steel/Al welds produced by magnetic field assisted laser  
1102 welding. *Optics & Laser Technology* 113:164-170
- 1103 84. LeBozec N, LeGac A, Thierry D (2012) Corrosion performance and mechanical properties of  
1104 joined automotive materials. *Materials and corrosion* 63 (5):408-415
- 1105 85. Wloka J, Laukant H, Glatzel U, Virtanen S (2007) Corrosion properties of laser beam joints of  
1106 aluminium with zinc-coated steel. *Corrosion Science* 49 (11):4243-4258
- 1107 86. Takehisa S, Iizuka T Galvanic Corrosion Related to Steel/Aluminum Dissimilar Joining  
1108 Tailored Blank. In, 2014. *Trans Tech Publ*, pp 1460-1467
- 1109 87. Jia L, Shichun J, Yan S, Cong N, Genzhe H (2015) Effects of zinc on the laser welding of an  
1110 aluminum alloy and galvanized steel. *Journal of materials processing technology* 224:49-59
- 1111 88. Chen S, Huang J, Ma K, Zhang H, Zhao X (2012) Influence of a Ni-foil interlayer on Fe/Al  
1112 dissimilar joint by laser penetration welding. *Materials Letters* 79:296-299
- 1113 89. Zhou D, Xu S, Peng L, Liu J (2016) Laser lap welding quality of steel/aluminum dissimilar  
1114 metal joint and its electronic simulations. *The International Journal of Advanced Manufacturing*  
1115 *Technology* 86 (5):2231-2242

- 1116 90. Zhou D, Xu S, Zhang L, Peng Y, Liu J (2017) Microstructure, mechanical properties, and  
1117 electronic simulations of steel/aluminum alloy joint during deep penetration laser welding. *The*  
1118 *International Journal of Advanced Manufacturing Technology* 89 (1-4):377-387
- 1119 91. Yang J, Yu Z, Li Y, Zhang H, Guo W, Zhou N (2018) Influence of alloy elements on  
1120 microstructure and mechanical properties of Al/steel dissimilar joint by laser welding/brazing.  
1121 *Welding in the World* 62 (2):427-433
- 1122 92. Sun J, Yan Q, Gao W, Huang J (2015) Investigation of laser welding on butt joints of Al/steel  
1123 dissimilar materials. *Materials & Design* 83:120-128
- 1124 93. Sierra G, Peyre P, Beaume FD, Stuart D, Fras G (2008) Steel to aluminium braze welding by  
1125 laser process with Al-12Si filler wire. *Science and Technology of Welding and Joining* 13 (5):430-  
1126 437
- 1127 94. Yang J, Li Y, Zhang H, Guo W, Weckman D, Zhou N (2015) Dissimilar laser welding/brazing  
1128 of 5754 aluminum alloy to DP 980 steel: mechanical properties and interfacial microstructure.  
1129 *Metallurgical and Materials Transactions A* 46 (11):5149-5157
- 1130 95. Zhang MJ, Chen GY, Zhang Y, Wu KR (2013) Research on microstructure and mechanical  
1131 properties of laser keyhole welding-brazing of automotive galvanized steel to aluminum alloy.  
1132 *Materials & Design* 45:24-30
- 1133 96. Xia H, Zhao X, Tan C, Chen B, Song X, Li L (2018) Effect of Si content on the interfacial  
1134 reactions in laser welded-brazed Al/steel dissimilar butted joint. *Journal of Materials Processing*  
1135 *Technology* 258:9-21
- 1136 97. Kah P, Vimalraj C, Martikainen J, Suoranta R (2015) Factors influencing Al-Cu weld  
1137 properties by intermetallic compound formation. *International Journal of Mechanical and*  
1138 *Materials Engineering* 10 (1):1-13
- 1139 98. Braunovic M (2007) Reliability of power connections. *Journal of Zhejiang University-*  
1140 *SCIENCE A* 8 (3):343-356
- 1141 99. Lee SJ, Nakamura H, Kawahito Y, Katayama S (2014) Effect of welding speed on  
1142 microstructural and mechanical properties of laser lap weld joints in dissimilar Al and Cu sheets.  
1143 *Science and Technology of Welding and Joining* 19 (2):111-118
- 1144 100. Liu YZ, Zheng BC, Jian YX, Zhang L, Yi YL, Li W (2020) Anisotropic in elasticity, sound  
1145 velocity and minimum thermal conductivity of Al-Cu intermetallic compounds. *Intermetallics*  
1146 124:106880

- 1147 101. Solchenbach T, Plapper P (2013) Mechanical characteristics of laser braze-welded  
1148 aluminium–copper connections. *Optics & Laser Technology* 54:249-256
- 1149 102. Braunovic M, Alexandrov N (1994) Intermetallic compounds at aluminum-to-copper  
1150 electrical interfaces: effect of temperature and electric current. *IEEE Transactions on Components,*  
1151 *Packaging, and Manufacturing Technology: Part A* 17 (1):78-85
- 1152 103. Zuo D, Hu S, Shen J, Xue Z (2014) Intermediate layer characterization and fracture behavior  
1153 of laser-welded copper/aluminum metal joints. *Materials & Design* 58:357-362
- 1154 104. Fetzer F, Jarwitz M, Stritt P, Weber R, Graf T (2016) Fine-tuned remote laser welding of  
1155 aluminum to copper with local beam oscillation. *Physics Procedia* 83:455-462
- 1156 105. Lerra F, Ascari A, Fortunato A (2019) The influence of laser pulse shape and separation  
1157 distance on dissimilar welding of Al and Cu films. *Journal of Manufacturing Processes* 45:331-  
1158 339
- 1159 106. Hailat MM, Mian A, Chaudhury ZA, Newaz G, Patwa R, Herfurth HJ (2012) Laser micro-  
1160 welding of aluminum and copper with and without tin foil alloy. *Microsystem technologies* 18  
1161 (1):103-112
- 1162 107. Mys I, Schmidt M Laser micro welding of copper and aluminum. In, 2006 2006. International  
1163 Society for Optics and Photonics, p 610703
- 1164 108. Esser G, Mys I, Schmidt MHM Laser micro welding of copper and aluminium using filler  
1165 materials. In, 2004 2004. International Society for Optics and Photonics, pp 337-342
- 1166 109. Weigl M, Albert F, Schmidt M (2011) Enhancing the ductility of laser-welded copper-  
1167 aluminum connections by using adapted filler materials. *Physics Procedia* 12:332-338
- 1168 110. Hu Y, He X, Yu G, Ge Z, Zheng C, Ning W (2012) Heat and mass transfer in laser dissimilar  
1169 welding of stainless steel and nickel. *Applied Surface Science* 258 (15):5914-5922
- 1170 111. Zhang X, Kobayashi N, Motegi Y, Yade N Porosity suppression in laser welding of pure  
1171 nickel and stainless steel. In, 2013. Laser Institute of America, pp 289-293
- 1172 112. Li Z, Yu G, He X, Li S, Zhao Y (2018) Numerical and experimental investigations of  
1173 solidification parameters and mechanical property during laser dissimilar welding. *Metals* 8  
1174 (10):799

1175

**Declaration of interests**

The authors declare that they have no known competing financial interests or personal relationships that could have appeared to influence the work reported in this paper.

The authors declare the following financial interests/personal relationships which may be considered as potential competing interests: